

Full length article

On the thinnest Al₂O₃ interlayers in Al-based nanolaminates to enhance strength, and the role of constraint

Thomas Edward James Edwards^{a,1,*}, Tianle Xie^{a,b,1}, Nicoló Maria della Ventura^a,
Daniele Casari^a, Carlos Guerra^{a,2}, Emese Huszár^a, Xavier Maeder^a,
Johann Jakob Schwiedrzik^a, Ivo Utke^a, Laszlo Pethö^{a,*}, Johann Michler^a

^a Empa, Swiss Federal Laboratories for Materials Science and Technology, Laboratory for Mechanics of Materials and Nanostructures, Feuerwerkerstrasse 39, 3602, Thun, Switzerland

^b College of Material Science and Engineering, Hunan University, 2 Lushan S Rd, Yuelu, Changsha, 410082, PR China



ARTICLE INFO

Article history:

Received 7 October 2021

Revised 4 September 2022

Accepted 6 September 2022

Keywords:

Al - Al₂O₃ PVD-ALD hybrid multilayer thin film deposition
Ultrafine-grained materials
Strengthening mechanism
Micromechanics
Finite element modelling (FEM)

ABSTRACT

Physical vapour deposition combined with atomic layer deposition was exploited to design a model system of UFG aluminium with a narrow grain size and shape distribution, including two types of interfaces (Al-Al & Al-Al₂O₃), with Al-Al grain boundary orientations exclusively parallel to the loading axis. This enabled isolated study of the strengthening mechanisms that ultrathin oxide layers would provide in a metal multilayer structure. The Al/Al₂O₃ crystalline/amorphous multilayers with 240 nm metal layers and oxide thicknesses in the range <1 nm–12 nm (i.e. to below the natural oxidation thickness), were microcompressed, yielding a pseudo-macroscopic yield strength of 532 MPa – over 100 MPa higher than the literature-conforming oxide-free reference. The homogenous co-deformation of the structure, with barrelling of the individual metal layers at the micropillar edges, results from the high bonding strength of the metal with its native oxide, meaning no failure or sliding at the interface, unlike previous Al/ceramic multilayer studies. Only the thicker (≥5 nm) oxide layers fractured in-plane: at locations coincident with vertical Al-Al grain boundaries. An analysis of contributions to the strength of these crystalline/amorphous metal/ceramic hybrid multilayers is carried out, identifying the Al-Al₂O₃ interface to be the crucial factor, rather than the in-plane tensile stiffness and considerable plasticity of ALD Al₂O₃ itself. The strengthening effect of the oxide layer was effective down to a layer thickness of just 0.5 nm.

© 2022 The Author(s). Published by Elsevier Ltd on behalf of Acta Materialia Inc.

This is an open access article under the CC BY license (<http://creativecommons.org/licenses/by/4.0/>)

1. Introduction

Nanoscale multilayered thin films consisting of alternating sub-layers of dissimilar materials have attracted extensive attention in recent years due to their unusual electrical [1,2], magnetic [3], optical [4], anti-radiation [5–7], thermal [8–10] and mechanical properties [11–20] as compared to their single component counterparts, and are hence very promising for engineering applications. The excellent mechanical properties are mainly attributed to the dense interfaces and interfacial structures amongst the dissimilar sublayers of the multilayers. Several studies have shown that the strength of the multilayers can reach up to one third or even half of the theoretical strength limit by reducing the individual layer thick-

ness h from sub-microns to a few nanometres [12,21–27]. Several classical models have been proposed to describe the mechanical behaviour of multilayers as the periodic bilayer thickness is decreased. At large layer thickness ($h > 100$ nm), the deformation of the multilayers is dominated by the pile up of dislocations at grain boundaries or other interfaces, and the deformation follows a Hall-Petch scaling law, with the flow strength increasing in proportion to $1/\sqrt{h}$ [12]. When $5 \text{ nm} < h < 100 \text{ nm}$, the strengthening mechanism generally follows a confined layer slip (CLS) model whereby the glide of Orowan-type loops or hairpin-like dislocations is bounded by individual layer interfaces [12]. When h is less than 5 nm, the strength and hardness of multilayers reach a peak value due to the interface barrier strength (IBS) mechanism

* Corresponding authors.

E-mail addresses: thomas.edwards@empa.ch (T.E.J. Edwards), laszlo.petho@empa.ch (L. Pethö).

¹ These authors contributed equally to this work and should be considered co-first authors.

² Present address: Swiss Cluster AG, Feuerwerkerstrasse 39, 3602, Thun, Switzerland.

which considers a single dislocation cutting across an interface. It is worth mentioning that the strength may drop down when the dislocation core dimension ($\sim 1\text{--}2\text{ nm}$) is on the order of the individual layer thickness [12,28].

Compared with the extent of studies to date on metal-metal multilayers with crystal-crystal interfaces, the number of studies regarding the deformation behaviour of metal-ceramic multilayers with crystal-amorphous interfaces are substantially more limited [29–31], particularly for cases where the thickness of the crystalline sublayer is much thicker than that of the amorphous sublayer. Indeed, most commonly for metal-ceramic multilayers studies, the individual layer thickness exceeds 20 nm; in such cases, microcompression determined that the multilayers deformed by exclusive plastic deformation of the soft metal layers (e.g. Al and Cu) with some extrusion at the free surfaces in between the ceramic layers [14,32,33]. This is known as impenetrable barrier theory, and has been elucidated in several computational studies [34–36]. The stiff and brittle ceramic layers undergo initial elastic deformation, then crack with increasing strain [37]. The high strength and hardness of the metal-ceramic multilayers to date is therefore solely the result of constraint imposed by the stiff ceramic layers on the plastic deformation of the soft metal layer. However, when individual layer thickness is decreased to a few nanometres, ceramic layers can become flexible and bear severe deformation without failing under compression [13–15, 32,38–41]. A special case of this is single layer graphene, whose immense strength and stiffness means that when multi-layered with Cu or Ni, it did not undergo plastic shearing but remained elastic [42,43]. Generally, the studies on metal-ceramic multilayer mechanics evoked thus far had metal-ceramic thickness ratios of 1:5 to 20:1; in contrast, the deformation mechanisms of multilayers is poorly understood when the metal/ceramic thickness ratio is from 25:1 to, say, 250:1, as will be studied here, i.e. the metal layer is several orders of magnitude thicker than the ceramic layers.

Often, metal-ceramic multilayers are prepared by magnetron sputtering (a form of physical vapour deposition, PVD) due to advantages such as almost no limitation in solid targets, the high deposition rate and tolerance for high vacuum conditions. However, the nucleation and island coalescence processes in the initial stage of Volmer-Weber film growth mean it is difficult to obtain uniform and continuous films below 5 nm thick, hence excluding studies of the mechanical behaviour of many ceramics as ultrathin layers within multilayers. Single layer graphene-metal multilayers are similarly complex to produce, requiring repeated transfers between vacuum deposition and wet chemistry steps [43]. Atomic layer deposition (ALD) instead provides us an excellent method to synthesise uniform, dense, continuous, and substrate conformal thin films, with precise thickness control at the Ångström scale due to its sequential and self-limiting surface chemical reactions. The combination of PVD and ALD without breaking vacuum has only recently been performed [44,45] and is successful in circumventing surface native oxidation of the metallic layers [44].

In this paper, Al-Al₂O₃ multilayers consisting of ALD deposited Al₂O₃ sublayers (with nominal thicknesses from 1 to 10 nm) between PVD deposited pure Al sublayers (250 nm thick) were fabricated using a hybrid custom-built PVD-ALD deposition system. A pure Al thin film of equal total thickness and same lateral grain size prepared by PVD was used for comparison. The mechanical behaviour of the Al-Al₂O₃ multilayers was investigated by micropillar compression tests to assess the performance of ultrathin embedded ceramic nanolayers. The microstructure analyses of the Al-Al₂O₃ multilayers before and after compression were performed using Scanning Electron Microscopy (SEM), Transmission Kikuchi Diffraction (TKD) and Transmission Electron Microscopy (TEM).

2. Experimental method

2.1. Sample production

The deposition of the Al-Al₂O₃ multilayer sample was carried out in a custom-built hybrid PVD-ALD deposition system that allows subsequent deposition processes to be conducted without breaking high vacuum between PVD and ALD chambers. This advanced technology was achieved by a chamber-in-chamber design in the hybrid deposition system, which is an important innovation as until now the PVD and ALD deposition processes were usually conducted in isolated vacuum chambers. This deposition system avoids surface native oxidation and the efficiency of multilayer preparation can be greatly improved. A detailed description of the custom-built PVD-ALD deposition system (Mantis Deposition Ltd., base model: QPrep500, United Kingdom) is presented in our previous work [44], along with the process parameters similarly employed for the current study. It is worth mentioning that the vacuum of this hybrid deposition system is always better than 1×10^{-5} Pa during the entire substrate transfer process between the vacuum chambers.

In this study, two Al-Al₂O₃ multilayers were fabricated by the hybrid PVD-ALD system consisting of eleven pure Al sublayers with nominal 250 nm thickness, alternating with ALD sublayers. For the first multilayer film, as in diagram Fig. 1b, ten ALD Al₂O₃ sublayers with thicknesses increasing from 1 to 10 nm (nominal thickness: 8 to 80 ALD full cycles) along the thin film growth direction in 1 nm increments were produced. The pure Al sublayers were deposited by direct current (DC) magnetron sputtering in the PVD chamber, and the Al₂O₃ sublayers were fabricated by alternatively exposing H₂O and trimethyl-aluminium (TMA) precursors in the ALD chamber (at 120 °C). In the second multilayer, Fig. 1d, ALD layers (from the substrate upwards) were: 8 full ALD cycles (1 nm nominal), 6, 5, 4, 3, 2, 1 cycles, followed by only a half cycle of H₂O, a half cycle of TMA, and finally a blank (sample transferred to ALD chamber, no deposition performed).

A 2.7 μm -thick pure Al thin film, Fig. 1a, was also prepared by DC magnetron sputtering in the PVD chamber. This Al thin film is actually constituted of 11 pure Al sublayers with the same nominal thickness of 250 nm. The interval times between each Al sublayer deposition varied from 0.5 h to 5 h with a 0.5 h increment, corresponding to the approximate durations of ALD deposition in the Al-Al₂O₃ (1–10 nm oxide) counterpart sample above. All of the samples were deposited on 4-inch single crystal Si <100> wafers. The details of the deposition parameters of the Al-Al₂O₃ multilayer and the pure Al thin film was described in [44].

Finally, to study the effect of lateral constraint on the mechanical behaviour of the Al-Al₂O₃ multilayer, an additional 1.2 μm thick W layer was DC magnetron sputtered on top of a subsection of the Al-Al₂O₃ multilayer sample, Fig. 1c, at room temperature. Deposition conditions were: 6.8×10^{-3} mbar at 15 sccm Ar flow, following 3×10^{-8} mbar base pressure, and 120 W at 0.3 A and substrate rotation at 2 rpm.

2.2. Taper-free square section micropillar fabrication

Taper free cuboidal micropillars with $2.5 \times 2.5\text{ }\mu\text{m}^2$ section and aspect ratio of 2–3 including Si pedestal were fabricated by Ga⁺ focused ion beam (FIB) milling using a Tescan Vela dual beam FIB workstation. A large square crater was milled outside of the pillar position at ion beam conditions of 30 kV, 10 nA. The pillar was milled and polished to the target size at successive currents of 1.1, 0.3 and 0.1 nA to minimize ion beam damage. Finally, the taper was removed from all sidewalls with a 1.5° over-tilt mill at 20 pA. The morphology of the taper free pillars of the Al-Al₂O₃ multilayer and the pure Al thin film are shown in Fig. 1e–h.

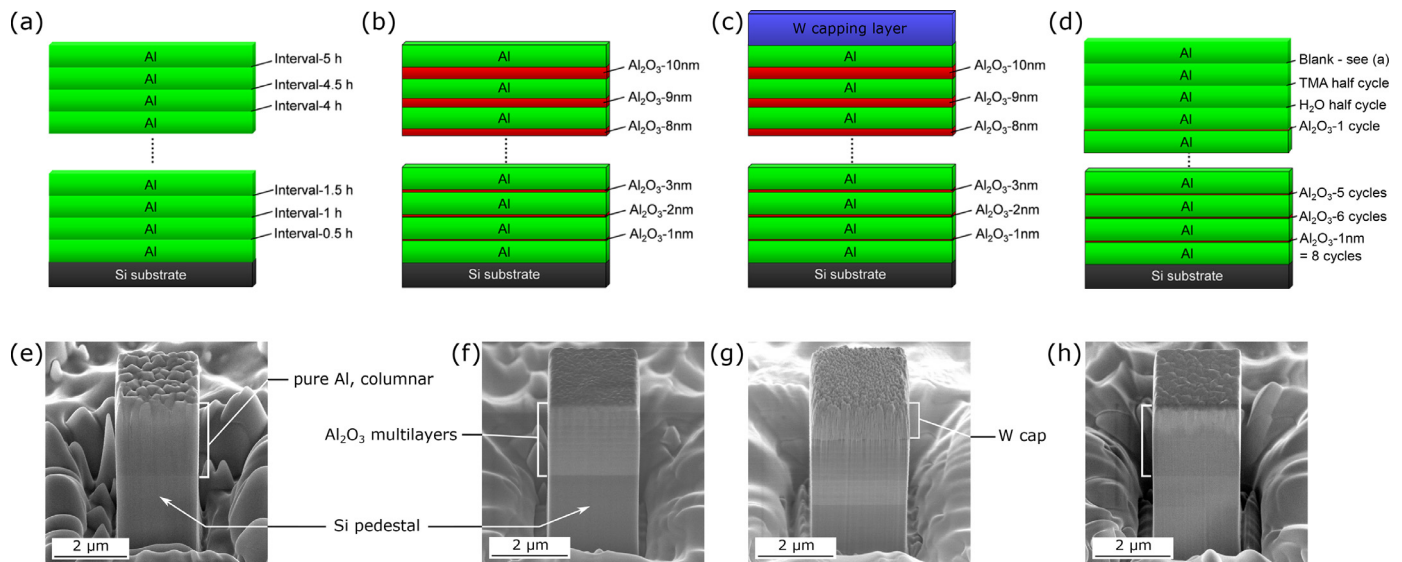


Fig. 1. Structure diagrams adapted from [44] of the (a) pure Al columnar-grained reference, (b) Al-Al₂O₃ multilayer film with 'thick' oxide layers (1 – 10 nm nominal), (c) the same multilayer with W capping layer and (d) Al-Al₂O₃ multilayer film with 'thin' oxide layers (0 – 1 nm nominal), along with (e,f,g,h) secondary electron images of taper-free square cross-section micropillars Ga⁺ milled from each.

2.3. Micro-compression tests

Micro-compression tests were performed using an in situ indenter system (Aleminis AG, Switzerland) inside a SEM (DSM 962, Zeiss, Germany) at room temperature. A 5 μm diameter diamond flat punch (Synton MDP, Switzerland) was used to compress at displacement rates of 2.7×10^2 to $2.7 \times 10^{-1} \text{ nm s}^{-1}$, corresponding to strain rates of the Al/Al₂O₃ (1–10 nm) multilayer sample of 10^{-1} – 10^{-4} s^{-1} , before correction for the indenter frame and Si pedestal-substrate compliance. The yield stress was extracted using a 1% strain criterion, in view of the experimental difficulty of applying the conventional macroscopic 0.2% criterion to micropillar deformation [46].

2.4. Characterization

The morphologies of the pillars were imaged using a cold field emission Hitachi S-4800 high resolution scanning electron microscope (SEM) at 1.5 kV, 10 pA, before and after the compression tests. The characterization of the cross-sectional microstructure was conducted on a transmission electron microscope (TEM, JEOL JEM2200fs, Japan) with a 200 kV accelerating voltage.

For lamella fabrication, pillars were surrounded on the top and side faces of the pillar by a protective e-beam gas injection system (GIS) deposited 100 nm thick Pt layer in a dual beam FIB workstation (Vela-Tescan), followed by a 2 μm thick ion-beam-assisted deposition of Pt. A standard FIB lift-out process on the same machine ensued to yield $\sim 100 \text{ nm}$ thick lamellae, as previously [44].

Transmission Kikuchi diffraction (TKD) was carried out using an Electron Backscattered Diffraction detector and associated acquisition and analysis softwares (EDAX, USA) within a Mira-Tescan SEM with a 20 nm step size. SEM beam conditions of 30 kV and 10 nA were used. The samples were tilted at -20° to the incident beam, at a working distance of 3 mm. Datasets underwent a single step nearest-neighbour noise reduction procedure. Lateral grain size was measured using a simple line intercept method without correction factor.

2.5. Finite element simulations

Finite element simulations of deformation, to assess the impact of the elastoplasticity of the oxide layers on the yield stress

of the total multilayer, were conducted as quarter-pillar models in Abaqus/Standard (Dassault Systèmes, France) with corresponding mirror boundary conditions about the two orthogonal planes parallel to the loading axis. The pillars were compressed by a rigid flat indenter with a surface friction coefficient of 0.1, which is common for diamond [47]. The complete 21 layers of the multilayer were modelled (240 nm thick Al layers, 1.2 nm–12 nm thick Al₂O₃ layers), along with the Si pedestal (3 μm high) with 500 nm root fillet radius and a sufficiently large Si substrate to yield a negligibly uniform stress state at its base. The aluminium layers were modelled as homogenous isotropic media with a 70 GPa Young's modulus and 0.34 Poisson ratio; for all multilayer combinations, yielding of Al at both 350 MPa and 200 MPa was evaluated, to cover the literature range, see Section 4.2, and without work hardening in light of the small grain size and the apparent sink properties of the Al-Al₂O₃ interfaces, again, see Section 4.2. The alumina layers were modelled with an elastic modulus of 170 GPa, as has been measured on ALD Al₂O₃ membranes at a thickness of 15 nm by bulge testing [48], a Poisson ratio of 0.24 [49] and a yield stress of 4.5 GPa as previously observed for thin amorphous alumina [41] with work hardening-free plastic flow to at least 8% plastic strain. The element thickness in the alumina layers was 0.6 nm. The room temperature anisotropic elasticity of (100) Si was similarly included, using values from [50].

3. Results

3.1. Microstructures of as-deposited multilayers

The cross-sectional TEM and TKD images of Al-Al₂O₃ multilayers and pure Al thin film are shown in Fig. 2. The Al-Al₂O₃ (1–10 nm) multilayer fabricated using the hybrid PVD-ALD deposition system consists of eleven PVD prepared Al sublayers (averaging 240 nm thick, from TEM imaging) and ten ALD-prepared ultrathin Al₂O₃ sublayers. The actual thicknesses of the individual oxide layers was reported previously [44] from high resolution TEM as $\sim 1.2, 2.4, 3.6 \dots 12.0 \text{ nm}$ (i.e. $\sim 20\%$ thicker than the nominal). High resolution analysis of the Al-Al₂O₃ multilayer with thinner oxide layers (1 nm, and below) will be the topic of a further publication, to better understand the structure of these sub-nanometre oxide layers, along with the considerable thermal stability of the present

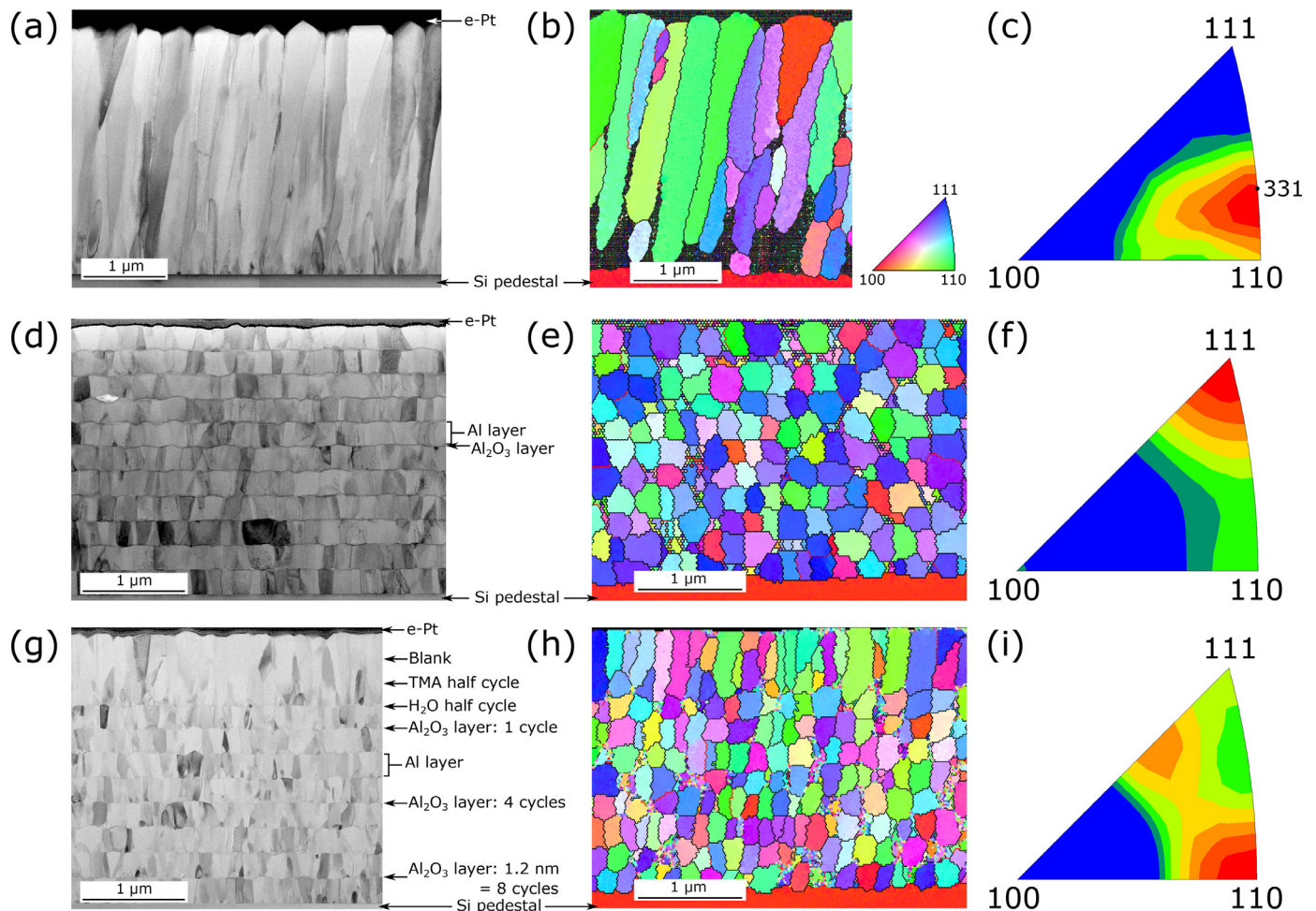


Fig. 2. (a,d,g) Cross-sectional bright field scanning TEM (BF-STEM) of the pure Al reference film and Al-Al₂O₃ multilayers, respectively, along with (b,e,h) transmission Kikuchi diffraction (TKD) maps of the Al grains in inverse pole figure colouring relative to the vertical (film normal) axis. High angle boundaries ($>15^\circ$) are indicated by black lines, whilst low angle boundaries ($5 - 15^\circ$) are in red. Texture of the as-deposited films relative to the film normal (pillar loading axis) is related by inverse pole figures in (c,f,i); a relatively weak texture of the pure Al reference is centred on approximately 331. The 1 – 10 nm thick oxide Al-Al₂O₃ multilayer's texture is again spread over a large range of orientations, with a median closer to 111. The 0 – 1 nm thick oxide Al-Al₂O₃ multilayer is also spread, with several local maxima in the 211 – 110 range. Texture was measured by TKD from a minimum of 50 grains (considerably more, shorter grains for the Al/Al₂O₃ conditions) with 5° discrete binning. Part reproduced with permission from [44].

Al-Al₂O₃ multilayers. Indeed, one may observe in Fig. 2g,h that even the thinnest amorphous Al₂O₃ sublayer (and the H₂O half cycle, but not the TMA half cycle or blank cycle) was sufficient to interrupt the columnar grain growth of each Al sublayer and replicated its surface roughness, stemming from the competitive columnar grain growth between adjacent Al grains. In contrast, the 2.7 μm thick pure Al thin film deposited with ten differing pauses presents a continuous growth mode of columnar grains normal to the Si substrate, such that many of the Al columnar grains stretch the entire film thickness.

The cross-sectional TKD patterns of multilayers sample confirm that the Al sublayers were isolated by the ultrathin Al₂O₃ sublayers, with nucleation anew of the metal grains at each layer. The Al sublayers presented a nanocolumnar grain structure where the columnar height is always equal to the layer thickness, and therefore the grain size is homogeneous, with a narrow distribution of the lateral grain size across all layers, averaging at 186 ± 15 nm for the thicker oxide multilayer, and 171 ± 11 nm for the thinner oxide one. The grain boundaries (GBs) within Al sublayers are mainly parallel to the thin film growth direction. TKD analysis of GBs indicates that most (93%) of the GBs amongst Al grains are high angle GBs. For the pure Al reference thin film, TKD identifies the columnar Al grains, most over 2 μm in height. Competitive growth at

the base of the film results in an increasing lateral grain size with film thickness; measured at three equispaced positions along the film thickness, the lateral size averages at 220 nm, though it is 260 nm at the top of the film. Again substantial lateral homogeneity in grain size is noted. The slight tilt of the columnar grains ($\sim 7^\circ$), all in a same direction, results from deposition using a single magnetron without substrate rotation. Texture relative to the film normal in all three samples was not strong, Fig. 2c,f,i, being spread over a wide range of orientations mainly between 111 and 110: the mode texture of the pure Al reference is approximately 331, whilst that of the Al/Al₂O₃ (1–10 nm) multilayer is 111.

3.2. Microcompression

3.2.1. Pure Al reference

SEM images of compressed reference pure Al micropillars are given in Fig. 3a,c. After compression to low, 8%, strain, Fig. 3a, slight barrelling of the pillar is seen as a deflection of the sidewalls of the Al relative to the sides of the Si pedestal. Plastic deformation of the Al film is achieved without obvious shearing of the entire Al film, or the appearance of slip bands on individual columnar grains. Relative to the top surface of the undeformed pillars, Fig. 1e, it is obvious that a considerable amount of the initial defor-

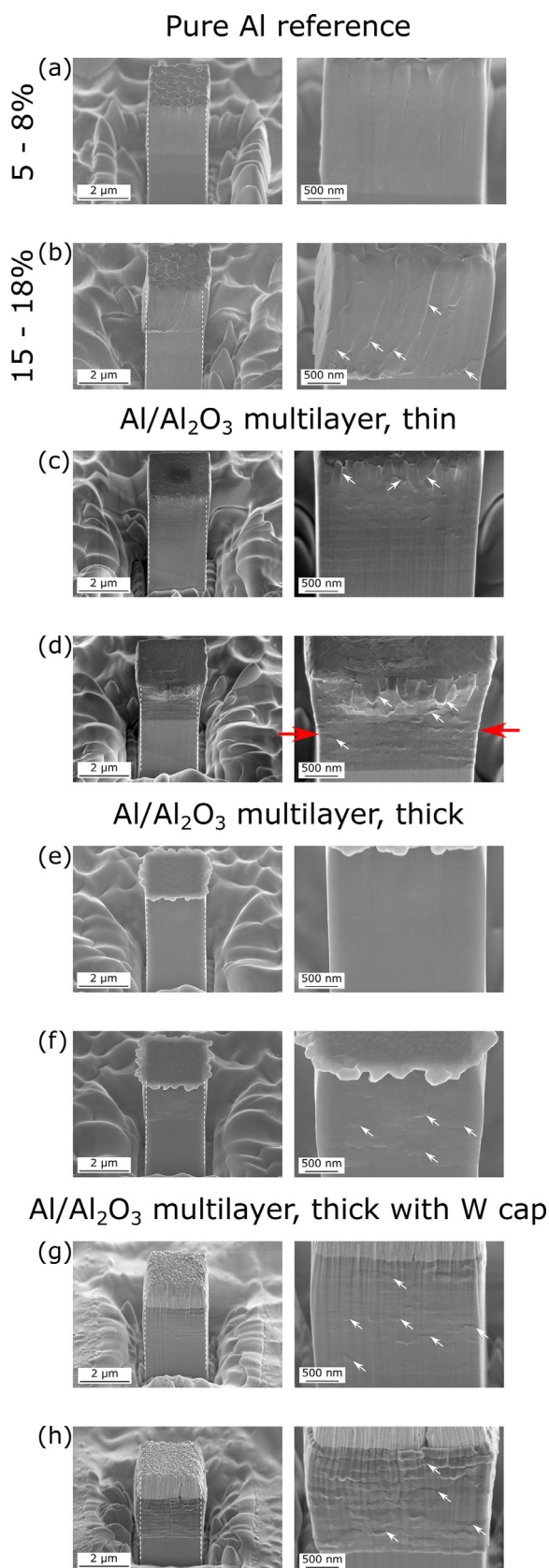


Fig. 3. Secondary electron SEM images of the morphology of the compressed pillars at 10^{-3} s^{-1} to (a,b,e,f) 5 – 8% strain and (c,d,g,h) 15 – 18% strain for (a,c) the pure Al reference film, (b,d) the Al/Al₂O₃ multilayer with 0 – 1 nm oxide layer thicknesses, (e,g) the Al/Al₂O₃ multilayer with 1 – 10 nm nominal oxide layer thicknesses, and (f,h) the latter multilayer with a W cap. Surface plasticity features of slip steps or grain boundary sliding are arrowed in white.

mation is focused in the flattening of the surface roughness, which serves to explain the particularly low loading modulus values measured in microcompression ($10.3 \pm 0.2 \text{ GPa}$, see later). Upon increased straining to 18%, Fig. 3c, plastic deformation is evidenced at the pillar surface by slip steps in the individual grains, as well as grain boundary sliding of entire columnar grains relative to their neighbours, leading to surface protrusions. Lateral deviation off the edge of the Si pedestal by the lower left section of the Al layer in Fig. 3c, near the Si-Al interface, indicates a deformation instability at high strain, with the direction likely determined by the tilt angle of the columnar grains. It is thought that this phenomenon does not affect the yielding behaviour of the pure Al reference film as it only occurs at higher strains. The lateral collapse of the lower portion of the layer erases any previous evidence of initial barrelling. Important to consider relative to the taper-free machining of the present pillars, is that there is neither a “mushroom effect” [15,51] at the top of the pillar (normally caused by stress concentration in a tapered pillar), nor inhomogeneous barrelling resulting from friction of the top of a tapered pillar with the diamond punch, much as Singh et al. reported in simulations of taper-free Al pillars [33].

Further analysis of an electron-transparent lamella of the 18% strained pillar in Fig. 3c by TEM and TKD, as shown in Fig. 4, indicates that, for the most part, the high angle grain boundary-separated, columnar Al grains remain. A larger lateral grain size in the upper region following compression, now 360 nm, which is beyond that required to maintain volume in plasticity, may indicate stress-induced grain boundary migration. An orientation dependence of the grain coarsening was not investigated by TKD due to the limited number of specimens, not allowing for a solid statistical analysis. The tilt of the whole Al layer is suggestive of grain boundary sliding between the columns, however there is no further direct evidence for this in post-mortem transmission imaging of the mid-section. It is apparent that from the morphology of the lower left of the Al layer, that interface debonding and sliding has not occurred at the Al/Si interface: rather, highly localised straining by lateral extrusion of Al. In this region, TEM imaging indicates a particularly high dislocation density, above that initially present from film growth, arranged in pile-up formation towards the grain boundaries – demonstrating the effectiveness of the high angle columnar grain boundaries in resisting dislocation transmission to neighbouring grains. Further, the overall fraction of high angle GBs was found to decrease, from 88% to 64%, whilst the local grain size in the region Fig. 4c is substantially smaller than the pillar average, and more equiaxed. This evidence points towards room temperature dynamic recovery (increase of low angle boundary fraction) and limited recrystallization at the high local strains of this compression instability, which is well-reported for pure Al [52].

3.2.2. Al-Al₂O₃ (1–10 nm) multilayer

Images of the compressed Al-Al₂O₃ (1–10 nm) multilayer pillars are in Fig. 3e,g. At both the lower (7%) and higher (16%) strain levels reported in the figure, pillar deformation was homogeneous, with minor barrelling, and no shear band formation or substantial extrusion of the Al layers. Slip steps in the Al layers are observed on the side surfaces of the pillars, whilst some bulging of the individual layers is apparent along the vertical layers – this is clearer in the TEM lamella below. It should be noted that initial stages of this study employed tapered cylindrical pillars by normal incidence of the Ga⁺ beam on the multilayer surface. The combined pillar taper and strain softening (see Section 3.2.3) of the multilayer led to a mushroom-shaped deformation morphology, illustrated in the Supplementary Material Fig. 1; this geometry is not effective to measure the mechanical behaviour of the individual oxide layers as a function of thickness. Using the taper-free pillars, Fig. 3, every Al layer is seen to contribute more equally to the total plastic

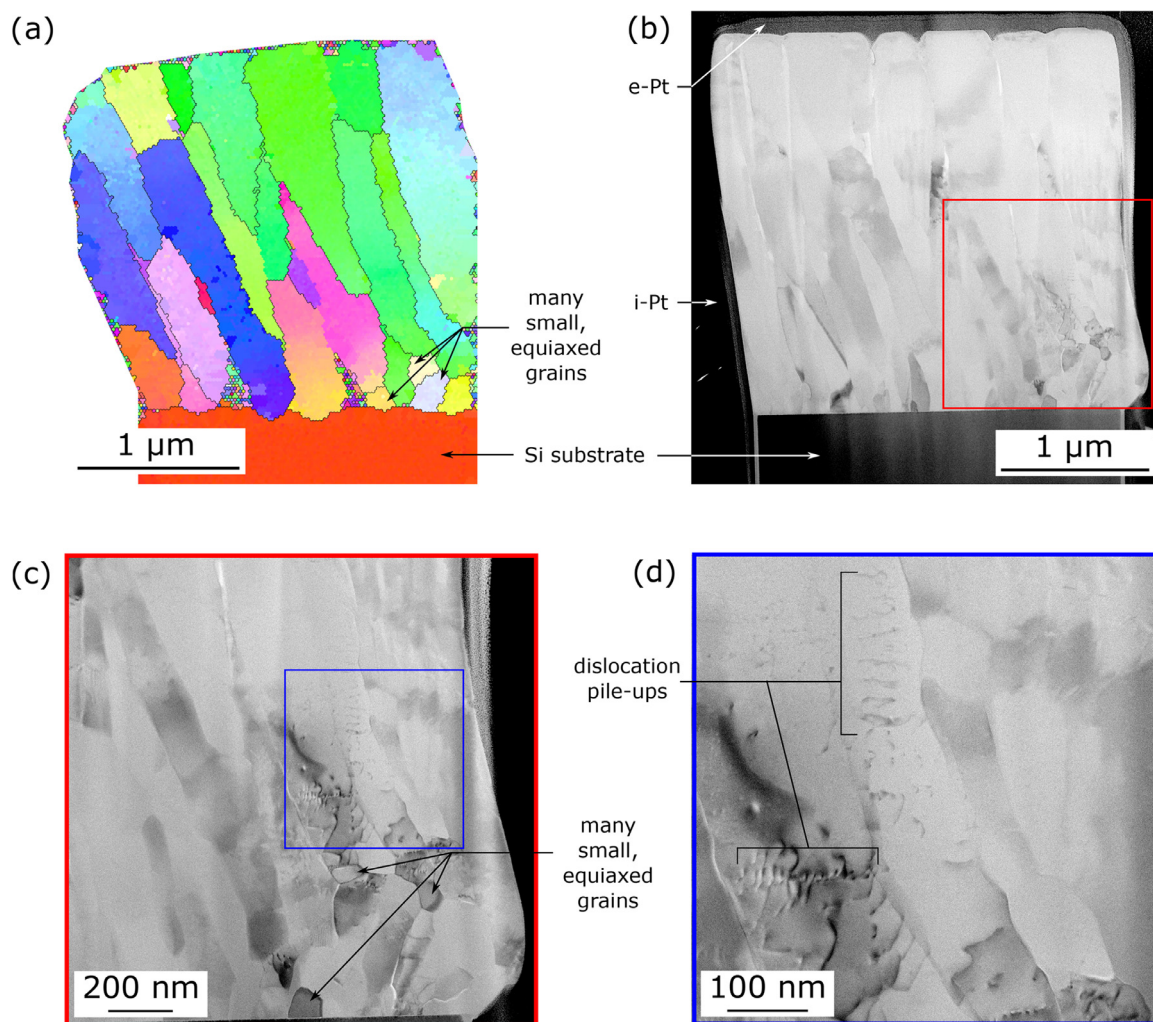


Fig. 4. (a) TKD and (b) BF-STEM images of a thin film extracted from the mid-depth of the pure Al reference pillar in Fig. 3c. In the details (c,d), the refined microstructure of the high plasticity region at the pillar base is highlighted, along with the numerous dislocation pile-up features. For TKD maps, the same IPF colour scheme, relative to the loading axis, is employed as in Fig. 2. High angle boundaries ($> 15^\circ$) are indicated by black lines.

strain. Again, no detachment was observed at the interface with the Si pedestal. When a W capping layer was included, Fig. 3f,h, to laterally constrain the upper surface of the multilayer pillars, the overall barrelling of the pillar at the mid-height Al layers relative to the upper one was, as expected, more substantial.

Again, TEM imaging and TKD measurements were undertaken, Fig. 5. Imaging confirms that no shearing or kinking across the layers occurs, even at the highest strains here: the structure after deformation retains the initial layer arrangement, with all Al and Al_2O_3 layers clearly distinguished: deformation remains homogeneous. No Al grain growth across the oxide layers was found, however the aspect ratio of grains does change. Indeed, the lateral grain size from TKD measurement, Fig. 5c,d, found the grain size distribution to evolve from being centred on 220 nm at 5% strain, to 240 nm at 15%. Again the high majority of high angle grain boundaries remains unchanged upon compression and the grains remain crystallographically distinct between the layers.

At the sides of the pillar, the Al layers are seen to individually bow outwards, see detail Fig. 5e, but without extrusion of the Al past the oxide along the full height of each layer. Indeed, the morphology indicates that no debonding occurs between Al and Al_2O_3 sublayers up to the highest strain levels tested here, for all Al_2O_3 thicknesses. Assuming pure plastic deformation of the Al layers, and hence conservation of volume for Al, the Al_2O_3 would be sub-

jected to a maximum in-plane biaxial tensile strain of 2.6% and 8.5%, at 5% and 15% overall compressive strain, respectively. The bowing of each Al layer at the pillar sides suggests that the oxide layers resist such in-plane strain, restricting the lateral straining of the bonded Al (a non-zero lateral tensile straining of Al_2O_3 must still occur to accommodate the barrelling of the pillar as a whole). Nevertheless, at 15% compressive strain, the in-plane tensile strain of the oxide layers is sufficient to cause their fracture; indeed measurement of lateral strain of the pillar from post-mortem TEM, Fig. 5b, finds this to vary between $\sim 0\%$ (i.e. at the Al-Si pedestal interface) and 10.5% tensile strain at the multilayer mid-height, where barrelling is greatest, hence locally exceeding the 8.5% expected from homogeneous, constraint-free deformation. Such fracture was observed in all Al_2O_3 layers above and including 5 nm thick (nominal), particularly at locations where vertical Al GBs intersect the Al- Al_2O_3 interphase, Fig. 5g. From the TEM images, one cannot rule out that grain boundary sliding be operative, but the grain geometries at the several strain steps indicate that GB sliding cannot be mediating most of the plasticity: the Al-Al GBs remain near-vertical throughout, and the large majority high angle character remains unchanged. In no case were dislocation lines seen to extend across the oxide layers; in Fig. 5h, one observes several dislocations with a single end coincident with the interphase – possibly pinned there. In fact, the thin-lamella samples of both the 5

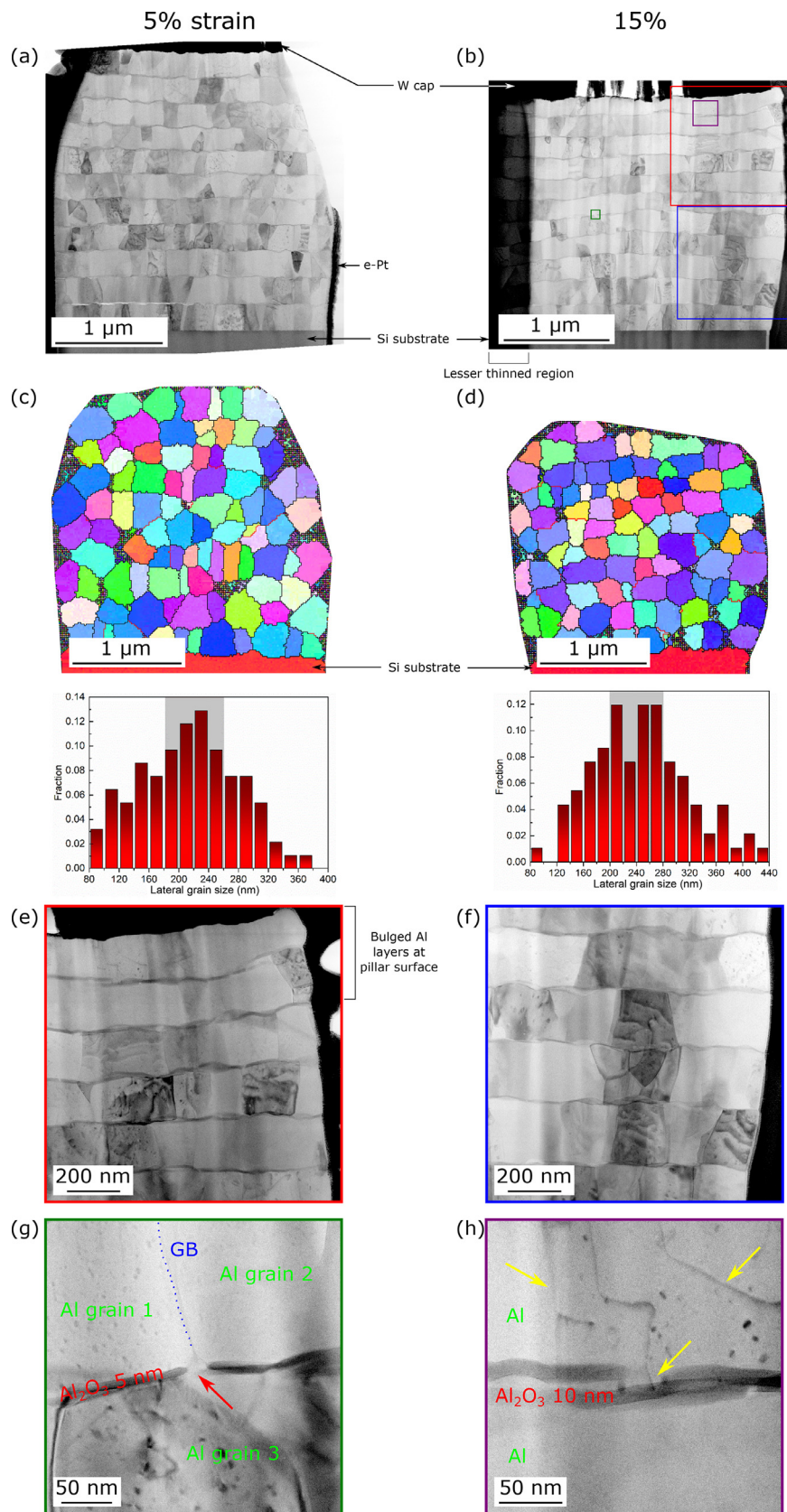


Fig. 5. (a,b) BF-STEM images and (c,d) TKD maps of thin film samples of the Al/Al₂O₃ (1 – 10 nm) multilayer with W cap, at 5 and 15% strain, respectively, again from the mid-depth of the pillars, as in Fig. 4. The histograms describe the spread of circular-fit grain diameters at each strain condition. For TKD maps, the same IPF colour scheme, relative to the loading axis, is employed as in Fig. 2. High angle boundaries ($> 15^\circ$) are indicated by black lines, low angle ($5 - 15^\circ$) by red lines. (e – h) Higher magnification details of (b), indicating (e,f) bulging of the Al layers at the pillar surface and a low or null dislocation density after unloading in approximately half the grains. In (g) the failure (arrowed in red) of the 5 nm (nominal) oxide layer occurs coincident with a vertical Al-Al grain boundary. (h) describes dislocations (arrowed in yellow) in the proximity of the oxide layer: one end of the dislocation arm lies at the oxide-metal interface, potentially pinned there.

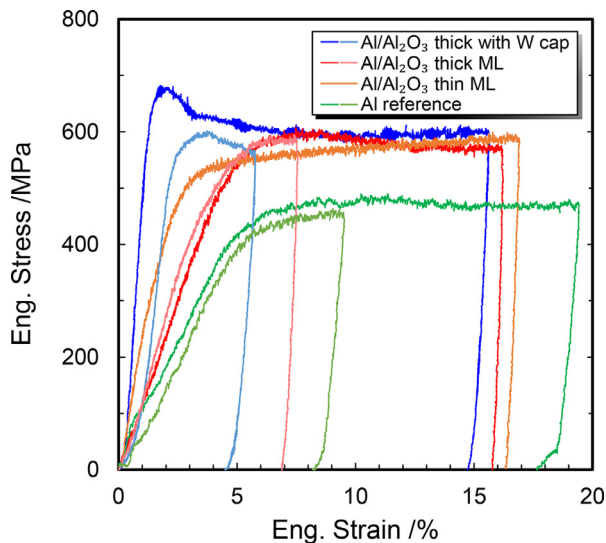


Fig. 6. An illustrative selection of engineering stress-strain curves of the pure Al reference and Al/Al₂O₃ multilayer micropillars, with and without the W cap, corresponding to the pillars in Fig. 3. Multiple tones of colour represent the range of stress-strain behaviour observed for that condition.

and 15% compressed multilayer pillars indicate a – maybe surprisingly – low dislocation density, despite the use of bright field STEM imaging, normally conducive to efficient contrast for a breadth of dislocation orientations and types. The majority of the grains appear to be entirely dislocation-free after unloading.

3.2.3. Al-Al₂O₃ (0–1 nm) multilayer

A considerable lateral bulging of exclusively the upper half of the Al-Al₂O₃ (0–1 nm) multilayer pillar is observed in Fig. 3b,d. This is particularly illustrative of the apparent strength benefit of the presence of the oxide layers, which appears in Fig. 3d to be effective above an oxide layer thickness of approximately 4 ALD cycles (~0.5 nm, arrowed in red in Fig. 3), limiting plasticity of the pillar through a reduced lateral expansion.

3.2.4. Yield strength at 10^{−3} s^{−1}

The four material conditions investigated were: the 2.7 μm thick pure Al reference film and the two Al-Al₂O₃ multilayer systems characterised in Section 3.1, as well as a version of the Al-Al₂O₃ (1–10 nm) multilayer, produced in the exact same deposition run as the former, but where an additional 1.2 μm thick W capping layer was added to impose equivalent lateral constraint on the top surface of the pillar as already achieved at the multilayer base by the sufficiently strong bond to the Si pedestal. Generally, at least five pillars were successfully compressed and analysed per material condition; Fig. 6 reports the loading curves, to several differing maximum strains per condition, demonstrating the good repeatability of the microcompression. The measured Young's moduli of the pure Al or Al-Al₂O₃ (1–10 nm) multilayer alone (e.g. after correction for loading frame compliance and elasticity of the Si pedestal and substrate) upon loading were low – averaging at 10.3 GPa for pure Al and 14.1 GPa for the Al-Al₂O₃ multilayer – but substantially higher for the multilayer with W capping layer: 46.5 GPa. This is a common feature of microcompression, and thought to result here from differences in surface roughness between the Al (higher roughness) and W layers (lower), as described and illustrated further in Sections 3.2.1 & 3.2.2. This is confirmed by consideration of the unloading moduli, which are 56.1 GPa, 129.2 GPa and 127.4 GPa respectively, i.e. much closer to the 70 GPa Young's modulus of bulk Al for the pure Al pillars following plastic densification of the upper regions of the films.

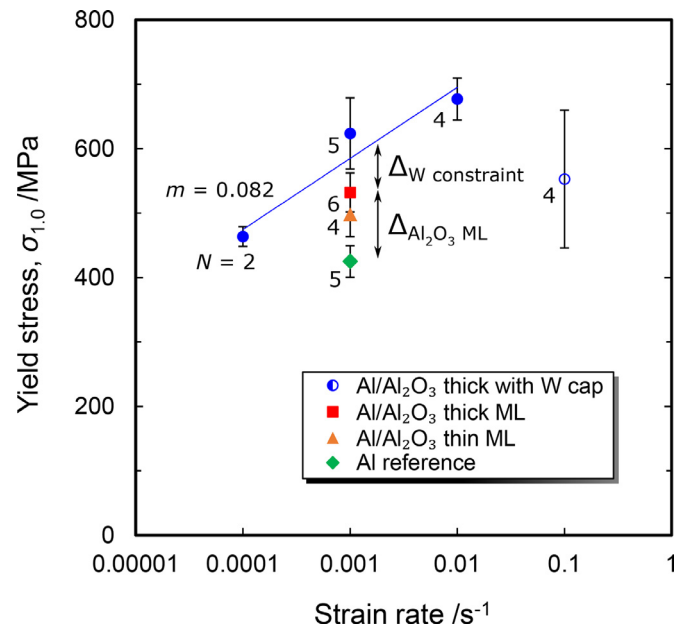


Fig. 7. Yield stress of the micropillars at 1% strain as a function of strain rate for the four material conditions studied here. The hollow circle indicates the data point was not used in the determination of the strain rate sensitivity coefficient, m ; the blue trendline is this logarithmic fit. The number, N , of repeats of each loading condition are indicated alongside the average values; error bars correspond to the standard deviations of these repeated measurements.

More interesting for the present study is the yield strength: 425 MPa for the Al reference film, increasing to 532 MPa with simple addition of the 1–10 nm thick Al₂O₃ ALD layers (average peak strength: 591 MPa), and further 624 MPa with the constraint of the W layer; the (0–1 nm) multilayer lies between pure Al and the thicker oxide multilayer, at 498 MPa. The data spread, summarised as standard deviations of measurement, are given in the summary graph, Fig. 7. In all cases, the loading curves are smooth – that is to say sudden load drops rarely occur, as are otherwise common for slip and twin operation during microcompression of single and oligo-crystals [46,53]. Whilst the Al reference displays an essentially null work hardening, the Al-Al₂O₃ (1–10 nm) multilayer with or without W cap has a stress peak shortly beyond the yield stress (~50–70 MPa above; a specific strain range under load is inconvenient to report for the peak stress occurrence, due to the low loading modulus in certain material conditions), followed by strain softening to a plateau at ~570 MPa in both cases – hence remaining well over 100 MPa above that of the pure Al reference (~440 MPa).

3.2.5. Strain rate sensitivity and activation volume

By performing microcompression tests on the double-constrained (W upper, Si lower) multilayer (1–10 nm oxide) samples at four log₁₀-equispaced strain rates in the range ~10^{−4} – ~10^{−1} s^{−1}, the strain rate sensitivity, m :

$$m = \frac{\partial \ln \sigma_y}{\partial \ln \dot{\epsilon}} \quad (1)$$

of the deformation could be extracted from the variations in the yield stress σ_y ($\sigma_{1.0}$ used here) and strain rate $\dot{\epsilon}$. One may note, Fig. 7, an anomalous yielding behaviour – i.e. above 10^{−2} s^{−1}, the yield stress is seen to decrease by over 100 MPa relative to that at 10^{−2} s^{−1}; the room temperature value for m of 0.082 was hence taken from the linear fit in the range 10^{−4} – 10^{−2} s^{−1}. The yield stress-strain rate data can further be used to extract the apparent activation volume V_{app} , which along with m determines an effective kinetic signature of the rate-controlling deformation mecha-

nism [54,55]:

$$V_{app} = \sqrt{3}k_B T \left(\frac{d \ln \dot{\epsilon}}{d \sigma_y} \right) \quad (2)$$

where k_B and T are the Boltzmann constant and temperature, respectively. Hence V_{app} was calculated here to be $6b^3$, where b is the Burgers vector of a perfect dislocation in aluminium, 2.864 Å.

4. Discussion

We start with a qualitative overview of the deformation morphology of the thin film samples, looking for clues for the active and controlling mechanisms, followed by a more in-depth quantitative analysis of specific mechanisms.

4.1. Deformation behaviour

The deformation characteristics of the pure Al reference sample here are broadly coherent with literature: on Ga⁺-milled 7 µm diameter micropillars of pure Al with equiaxed 700 nm grains, Xiao et al. [56] measured a yield of 320 MPa at 10⁻³ s⁻¹; this is analysed further in the next section. Li et al. [57] similarly found lateral grain coarsening of their nanocolumnar Al-based grains in the upper half of the pillar in this microstructural orientation. If instead they compressed normal to the long axis of the grains, the strength decreased 20%, and deformation was characterised by intergranular shearing along ~45° planes and eventual fracture along this path [57]. The ~7° tilt of the columns here also leads to some GB sliding character. One disparity of the present 220 nm pure Al relative to larger equiaxed grained nanocrystalline (≥ 700 nm diameter [56,58]) or microcrystalline Al is in the work hardening behaviour, which normally leads to a continuously increasing flow stress until sample failure. Instead, here, as in other nanocolumnar grain studies (≤ 450 nm [59]), there is no work hardening: the engineering stress is constant until over 20% compressive strain – our selected loading limit.

Relative to established deformation modes [16], the behaviour of the Al-Al₂O₃ (1 – 10 nm) multilayer pillars may be described best as a combination of homogeneous co-deformation (barrelling of the full 2.7 µm thick stack) and individual metal layer barrelling (bulging of the Al layers at the pillar edge). This kind of deformation behaviour is different from that in other metal-ceramic multilayers investigated (e.g. Al-SiC multilayers [32,33], Cu-graphene [43]), where for 50 – 200 nm metal layers, the metal is extruded from the lateral micropillar surface during compression, with complete loss of nearest-neighbour volumes across the metal-ceramic interface (apparent sliding). This important difference is a result of the high bonding strength of the Al-Al₂O₃ interface, where the work of separation is up to 9.7 J m⁻² for Al/Al₂O₃ depending on exact interface stoichiometry [60] – noting an oxygen overstoichiometry in ALD (amorphous) a-Al₂O₃ deposited at 120 °C (O:Al is 1.59:1 (at.) and H content is 10.1 at.% for a density of 3.0 g cm⁻³ in [61]). This compares to only 1.52 J m⁻² for Al/TiN [62], 4.74 J m⁻² for Al/SiC [63], and ~3.9 J m⁻² for analogous system Ti/TiO₂ [64]; as experimental or simulation data is lacking for amorphous oxides on crystalline metal, we state an equally weighted average of separation energies across reported crystalline oxide structures and orientations. This interface is achieved here with low impurity concentration by PVD-ALD deposition without breaking vacuum, and this despite waviness of the metal layers resulting from competitive grain growth: the conformity of ALD is an asset here. Recently, it has been reported that sub-10 nm ceramic interlayers can undergo extensive deformation [37,65]; in particular, amorphous Al₂O₃ produced by pulsed laser deposition [41] may yield at 4.5 GPa followed by tensile flow to 8% plastic strain (i.e. 15% total strain). This plasticity is a second fac-

tor that enables the co-operative deformation of the Al-Al₂O₃ binary, where 50 nm SiC or graphene layers would otherwise remain purely elastic, followed by eventual brittle fracture in the case of SiC [37] and TiN [40]. Indeed, in the present study, oxide thicknesses below 5 nm did not fracture, even where the in-plane biaxial tensile strain could reach up to 10.5%. It is a notable finding that in none of the oxide thicknesses studied here did plasticity of the amorphous layer occur by shear localisation, based on TEM observations of the geometries of deformed layers: no abrupt vertical displacements of the a-Al₂O₃ layers were found. Where the oxide layers were thicker than 5 nm and did eventually fracture, the coincidence with Al-Al vertical GBs suggests that incompatibilities between the Al grains, either due to differentially orientated elastic stiffness anisotropies, or poor slip transmission at the GB, is the cause for local stress concentration and hence oxide failure.

The arrangement of dislocations in the multilayer pillars after deformation is worth consideration: although the grains size is above the minimum necessary for Taylor hardening to be active [12], most grains appear dislocation-free after unloading. Furthermore, of the few that remain, several appear to be end-pinning at the metal-oxide interface. This suggests the metal-oxide interface may act as a dislocation sink, discussed further in Section 4.2.3, and that unlike the Al reference where dislocation pile-ups are imaged, Taylor hardening may be repressed in the multilayer sample by the low dislocation density. This importance of the metal-oxide interface is reinforced by the observation of the effectiveness of the oxide layer down to a thickness of just ~0.5 nm. The absence of any dislocation pile-up and emission features across the oxide layers in post-mortem TEM also indicates a certain degree of independence of deformation of the Al layers, at least relative to common crystal-crystal strain transmission mechanisms. As in many previous ultra-fine grained (UFG) Al studies, the predominance here of high angle boundaries should further increase strength through plastic incompatibility between neighbouring grains. Altogether, these lead to a 107 MPa strength increase relative to the pure Al reference, solely achieved by including the 1.2 – 12 nm thick oxide layers, i.e. without any reduction in the lateral grain size, and even an apparent loss of Taylor hardening. To better understand the source of this strength increase, the individual contributions to strength will be assessed in the following sections.

A final point to note in the deformation behaviour of the Al-Al₂O₃ (1 – 10 nm) multilayer sample is the large, 124 MPa, decrease in yield stress between strain rates of 10⁻² and 10⁻¹ s⁻¹. This may relate to a rate-limited deformation process, which is suppressed at 10⁻¹ s⁻¹, such as the formation of long-distance shear bands as in some nanolayered crystalline films and metallic glasses [66,67] – however shear band formation is notably absent at all strain rates here. In this strain rate range, no mechanistic transition is expected for nanocrystalline or UFG Al [68]. For the oxides layers, the fracture of alumina, and many other ceramics, is relatively strain-rate independent at quasi-static rates (see [69] in the range 10⁻⁴ – 10⁰ s⁻¹). The source of this strain rate anomaly is therefore unclear: it could relate to the specific processes occurring at the metal-oxide interface, discussed further in section 4.3.3; testing to higher strain rates is required for further characterisation.

4.2. Strengthening

First, we consider strength levels expected from conventional metallurgical strengthening, followed by that achieved with the addition of impenetrable barrier theory, or by alternative crystalline-amorphous metal-oxide dissimilar interface mechanisms. Further comment on the extrinsic geometric constraint by the W capping layer and the aspect ratio of the pillar is given in the Supplementary Material.

4.2.1. Conventional mechanisms in metallurgy

For a generalised metallic system, the yield strength, σ_Y , may be expressed as:

$$\sigma_Y = [\sigma_0^i + \sigma_{HP}^i + \sigma_{Tay}^i + \sigma_{SSS}^i + \sigma_{Oro}^i + \sigma_{twin}^i + \sigma_{coh}^i + \sigma_{ord}^i]^{1/i} \quad (3)$$

where σ_0 , σ_{HP} , σ_{Tay} , σ_{SSS} , σ_{Oro} , σ_{twin} , σ_{coh} , and σ_{ord} are contributions from the intrinsic lattice friction, grain boundaries (Hall-Petch), dislocation networks (Taylor hardening), elements in solid solution, oxide or precipitate dispersion (Orowan bowing), twins (similar to Hall-Petch), coherency (lattice misfit between phases with compatible structures for dislocation transmission) and precipitate superlattices (order strengthening), respectively. The exponent i is commonly assumed to be 1, but values anywhere between 1 and 2 have been identified previously [70–72], as several strengthening mechanisms are not fully independent of each other, and ranges of particle sizes may exist in a matrix [71], for example. Hence in the present analysis, the extrema values for σ_Y at $i = 1$ and $i = 2$ will be evaluated. The grain size, d , above 200 nm in both sample types studied here is within the scope of Hall-Petch scaling law: the confined layer slip (CLS) model is generally reported to only contribute significantly at d below $\sim 50 - 100$ nm [12]. This is confirmed by the observation here by post-mortem TEM of dislocation pile-up features in the pure Al sample, Fig. 4d.

For the columnar-grained pure Al reference sample, several terms in (3) are null: the impurity concentration of the sputtered metal is low (e.g. Ar < 0.02 at.% [73]), such that σ_{SSS} is presumably negligible, TKD indicates no twin population, annulling σ_{twin} , whilst no second phase exists, eliminating σ_{Oro} , σ_{coh} , and σ_{ord} . The terms σ_{HP} and σ_{Tay} may be expressed as [74–76]:

$$\sigma_{HP} = kd^{-1/2} \quad (4)$$

$$\sigma_{Tay} = M\alpha Gb\sqrt{\rho} \quad (5)$$

where k is the Hall-Petch coefficient, M is the Taylor factor ($M = 3$ for randomly orientated face-centred cubic polycrystal – used here), G is the shear modulus (~ 26 GPa for Al), b is the Burgers vector (0.2864 nm), α is a constant (0.24) and ρ is the dislocation density. Literature is rich with mechanical data on microscopic and ultra-fine grained (UFG: diameter $\sim 5 \mu\text{m} - 100$ nm) aluminium [76,77]. Commonly σ_x is plotted against $d^{-1/2}$, where x is the applied plastic strain, such that the slope k may be evaluated (assuming linearity, $i = 1$) at successive strain values; variable values [78] of k on x , i.e. k_x , highlight the interplay, in reality, between grain-size and Taylor hardening. Explicitly:

$$\sigma_x = [\sigma_0^i + (k_x d^{-1/2})^i + (M\alpha Gb\sqrt{\rho_x})^i]^{1/i} \quad (6)$$

Several studies report $\sigma_0 \sim 10$ MPa [79]. From the data in Fig. 8 for $\sigma_{0.2}$ ('yield stress', at 0.2% strain) of macroscopic annealed test specimens, a transition in k is identified at $d \sim 10 \mu\text{m}$, potentially related to the transition from a core-shell Hall-Petch model [80,81] to a monolithic one; $\sigma_{0.2}$ of annealed samples being used, it may be assumed the Taylor component is negligible there ($\rho_0 < 4.0 \times 10^{12} \text{ m}^{-2}$ at 0.2% strain [82], so $\sigma_{Tay} < 11$ MPa). Hence in the grain size range of the present study, $k_{0.2} \sim 133 \text{ MPa } \mu\text{m}^{1/2}$. Additionally reported in Fig. 8 are annealed Ga^+ milled micropillars [56,58]. The equal channel angular pressed (ECAP) samples display a similar k to the macroscopic samples, yet retain a stress offset of ~ 30 MPa (Δ_{MP} in Fig. 8); this is likely caused by the micropillar loading geometry, whereby the low lateral compliance of the pillar base leads to a heightened yield stress – see discussion in 4.3.1. The $\sigma_{0.2}$ of the 700 nm high pressure torsion (HPT) sample [56] lies substantially above the rest: the authors report issues with microstructure analysis which may indicate a bi-

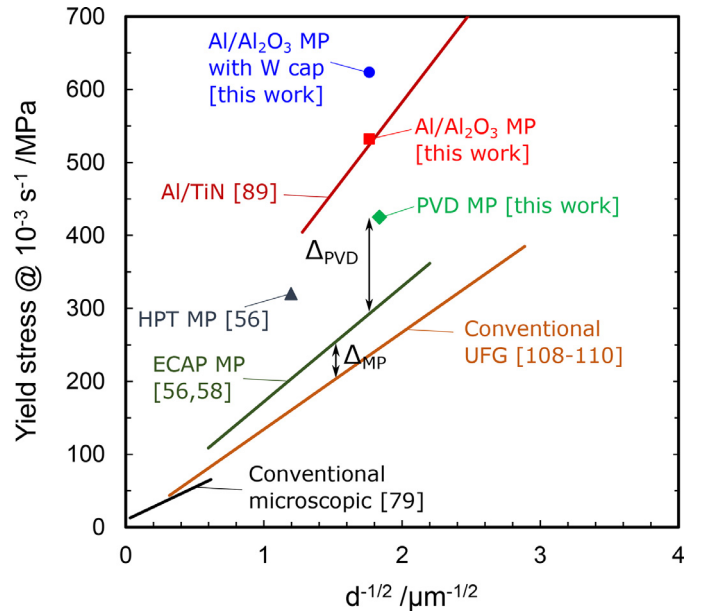


Fig. 8. Yield stress of pure annealed aluminium at 10^{-3} s^{-1} against inverse square root grain size [56,58,79,108–110]. Lines are linear fits to the literature data indicated; the ECAP micropillars trendline is extrapolated. PVD data [89] is from the as-deposited condition (i.e. not annealed, unlike other processing). 'Conventional' refers to macroscopic mechanical testing. 'MP' refers to data from Ga^+ FIB-milled micropillars. Other acronyms are defined in the main text. Data from nanoindentation [89] is converted to a yield stress according to $\sigma_Y = H / 3$. For multilayer systems, the corrected grain size is employed, converted from metal layer thicknesses to an effective (111) plane length, considering the 111 texture, as in Section 4.2: $d_{\text{corr}} = 1.22t_{\text{Al}}$ for [89]. Only the $\text{Al}/\text{Al}_2\text{O}_3$ multilayer with nominal oxide layer thicknesses 1 – 10 nm is plotted.

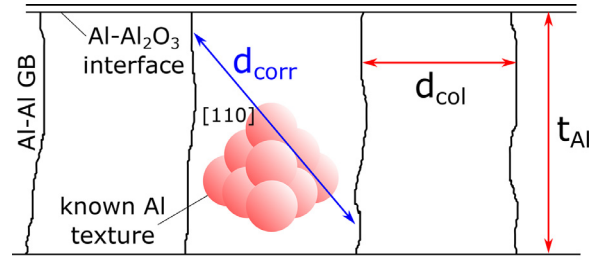


Fig. 9. Schematic of the metal columnar diameter, d_{col} (respect. metal layer thickness, t_{Al}), correction procedure to calculate the effective equiaxed grain size, d_{corr} , for the columnar grained model system studied here.

modal grain size distribution, and a high density of additional non-equilibrium sub-grain boundaries, with potentially even nanocrystalline (< 100 nm diameter) grains separating the 700 nm ones.

For the model films of the present study, one may consider a correction factor allowing conversion of the lateral columnar grain width, d_{col} , into a Hall-Petch-appropriate dislocation-perceived length, d_{corr} (on (111) planes, in the [110] direction, see Fig. 9), equivalent to the diameter of equiaxed UFG grains for ease of comparison. This is dependant on the out-of-plane texture: e.g. for an exact 101 orientation, this would be $d_{\text{corr}} = 2/\sqrt{3}d_{\text{col}}$, whilst for 111 (mode of $\text{Al}/\text{Al}_2\text{O}_3$ here) it is $d_{\text{corr}} = \sqrt{3}d_{\text{col}}$; for 331 this is estimated at $d_{\text{corr}} \approx 1.35d_{\text{col}}$ by interpolation. The data point for the Ga^+ milled micropillar Al reference sample ($d_{\text{corr}} = 297$ nm: mode orientation ~ 331) of the present study lies ~ 120 MPa above the annealed ECAP line (Δ_{PVD} in Fig. 8), which is indeed consistent with the higher dislocation (and point defect) density of as-sputter deposited films: $\rho_0 \sim 4.0 \times 10^{14} \text{ m}^{-2}$ [83], such that $\sigma_{Tay} \sim 107$ MPa. Hence Eq. 6 predicts a strength between 361 MPa ($i = 1$) and 267 MPa ($i = 2$): the upper bound is close to the 425 MPa

measured here if the further ~ 30 MPa supplement of the micropillar geometry observed previously for this material [56,58] is considered.

In another study [59] on nanocolumnar sputter deposited Al, the measured yield stress for 450 nm diameter columnar Al was only ~ 200 MPa. However, the pillar diameter used was $1\ \mu\text{m}$; therefore, unlike the present and the above study of Wheeler et al., the criterion of the pillar diameter being at least ten times larger than that of the average grain is not achieved. Hence in such oligocrystal pillars, the effect of lateral constraint of neighbouring grains (i.e. a constituent of Hall-Petch strengthening) is not consistently maintained: in many cases dislocations in an inner grain can escape at a free surface. A lower yield strength, part-way between a 450 nm UFG bulk and a single crystal would therefore indeed be expected.

Based on Eq. (6), at $\rho_0 \sim 4.0 \times 10^{14}\ \text{m}^{-2}$, strength in the range 352 ($i = 1$) to 256 MPa ($i = 2$) would be predicted for the Al/Al₂O₃ (1 – 10 nm) multilayer with $d_{\text{corr}} = 322\ \text{nm}$ – far short of 532 MPa measured, particularly considering the fact that post-mortem TEM of this system finds grains to be mainly dislocation-free, suggesting that Taylor hardening is not substantially active, further reducing the matrix strength (e.g. decreasing $\rho_0 \sim 4.0 \times 10^{14}$ to $4.0 \times 10^{12}\ \text{m}^{-2}$ as above, σ_{Tay} drops from 107 to 11 MPa). This pseudo-macroscopic strength is achieved despite the multilayer film being 97.8 at.% Al and containing 97.5 vol.% Al grains, which are solute-free and precipitate-free. This yield strength remains competitive with many top-of-class Al-alloys [84] – without yet considering any solution or precipitate strengthening of the Al grains, or the potential for further grain refinement. The impact of the loading geometry on the measured strength should be considered however – see further discussion in Supplementary Material.

In short, the 107 MPa higher strength compared with the pure Al reference requires additional strengthening terms than in Eq. 6. Although the oxide layers thickness are below 12 nm, the CLS model usually applied at this length scale [12] is not appropriate as Al₂O₃ here is not crystalline. Instead, for amorphous structures, alternative size effects in shear band kinetics exist; more often studied in metallic glasses, this leads to a suppression of shear banding below a critical size as the local volume is insufficient to accumulate sufficient energy for shear band formation [85], e.g. for Pd₈₂Si₁₈ this means homogeneous plasticity below a 9 nm film thickness [86]. In section 4.3, we will first consider whether the measured strength can be explained entirely by impenetrable barrier theory, considering also the elastoplasticity of the amorphous oxide layers themselves; indeed, unlike other metal/ceramic systems, e.g. Al/TiN & Al/SiC, the high bond strength between Al and Al₂O₃ mean the oxide layer is laterally drawn by the plasticity of the metal layers. Finally, we will consider whether the crystalline-amorphous character of the interphase may contribute a unique further benefit.

4.2.2. Impenetrable barrier layers: modelling and experiment

The basic theory of impenetrable barrier theory in crystalline plasticity, whereby an internal or external surface impedes strain transfer, has been established now for several decades [34–36]. Strain gradient crystal plasticity and discrete dislocation dynamics simulations have robustly captured the effect of impenetrable barrier layers on the strength of FCC crystalline layers. In fact, these models predict that perfect impenetrability could lead to a greater proportional strength increase (60% for a layer thickness divided by three [34]) than observed here. However, to achieve such levels of impenetrability practically, significantly thicker layers are required than the 0.5 nm effective thickness of Al₂O₃ found here. Indeed, in a previous study [87] of the Al/Al₂O₃ multilayer system (~ 5 nm Al₂O₃ layers), the strength over 500 MPa here was not achieved even at a metal layer refinement of 50 nm thick, whereas in micro

electromechanical device-based loading by de Boer et al. [88] of ~ 200 nm free-standing Al films capped on both sides by an oxide layer, strengths of 600 MPa were measured. This difference may be related to the nature of the oxide layers: in the former, deposited by pulsing oxygen gas during evaporation of Al, the low energy of deposition likely led to semi-crystalline oxide layers, as elsewhere [13], unlike the amorphous oxide here (ALD), although the structure was not specifically reported by the authors in [87]. In the Al/TiN [89] and Al/Si₃N₄ [31] systems, an identical strength to the present for this grain size was found to within 10% experimental error (by interpolation, after converting nanohardness, H , to a yield strength via $\sigma_Y = H / 3$); however, the Al content there was below 84 at.% due to the ~ 25 nm crystalline TiN or 250 nm Si₃N₄ layers required to achieve this strength. However, where the TiN layers were considerably thinner (2 nm), they were not impenetrable as slip transmission from Al into them (co-deformation) did occur [65].

To contextualise, in the metal/ceramic Cu/graphene and Ni/graphene multilayer systems developed by Kim et al. [43], the significant strengths (up to 4 GPa) achieved were attributed to the high in-plane stiffness of the graphene layers, which altogether impeded the glide of dislocations between the metal layers; this was supported by molecular dynamics modelling which found dislocations to be halted at one metallic monolayer before the graphene interface. That is to say, the graphene layer is a perfectly impenetrable barrier.

Conflicting variations of the activation energy for flow (by nanoindentation) have been reported upon reducing the metal grain size to below ~ 25 nm [37,90]. In Al/SiC, the activation energy is found to increase – reportedly a sign of dominant diffusion-controlled processes at the high density of interfaces; whilst in Cu/TiN this activation energy decreases – apparently indicating ‘co-deformation’ of the metal-ceramic layers, similarly evoked for the Al/SiC system [37]. Equivalent variable temperature testing of the present system is needed to assess specific processes at the Al-Al₂O₃ interface during deformation via the activation energy.

In fact, it is worthwhile to consider separating the effect of the strong interfacial adhesion and elastoplastic deformation of the oxide layers on the yield stress and work hardening behaviour, from that of crystal plasticity inhibition – the impenetrable aspect of the hard layers. We achieve this here by finite element modelling (FEM): any existing or straightforwardly envisageable analytical approaches are limited to purely elastic behaviour [91,92]. The aim here was to estimate the maximum contribution the oxide layers could achieve; hence perfect bonding between the metal and oxide layers, and without possible fracture of the oxide, was maintained throughout – much as experiment indicates to be the case for the thinner oxide layers, the thicker layers cracking in-plane at higher strains. Additionally, homogeneous, isotropic plasticity of the metal layers was assumed, not crystalline plasticity: this effectively removes the ‘impenetrable barrier’ effect from the calculations. Whilst the interface with the diamond punch was simply frictional, the interface between Al and the Si pedestal may locally debond (mode II/III) upon loading, even if this detail is not captured by the present imaging. To determine the impact on the loading curve and deformation morphology of this phenomenon, calculations were executed at two extremes: firstly with perfect bonding, and secondly with purely frictional sliding with a coefficient of friction of 0.6, which is common for metals sliding on SiO₂ glass [93]. As seen in the Supplementary Material Fig. 2, the boundary conditions at the multilayer-pedestal interface have a negligible impact on the overall deformation properties; for its simplicity, the perfect bonding condition was maintained elsewhere.

The microcompression of four multilayer arrangements was simulated: a pure Al reference, as experimentally, the 1.2 – 12 nm

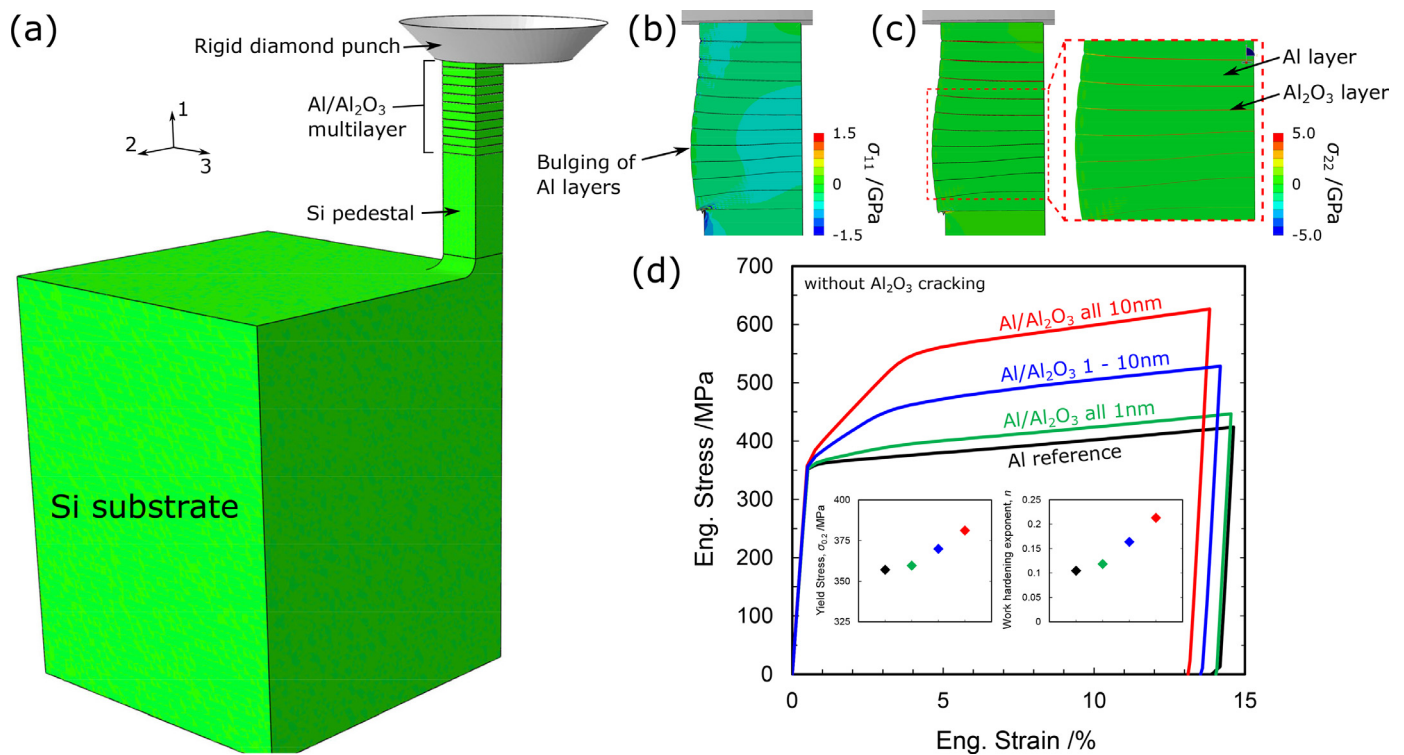


Fig. 10. Finite element simulation of compression of the multilayer system to evaluate the impact of elastoplasticity of the oxide layers on the yield strength: (a) overview of quarter-model employing mirror-plane boundary conditions in 1–2 and 1–3, with a large Si substrate to achieve far-field loading condition, a Si pedestal and the Al/Al₂O₃ appropriately scaled the TEM measured dimensions (not nominal). Details of the normal stress fields of the 1–10 nm Al₂O₃ pillar at ~14% strain, under maximum load, relative to (b) the loading axis and (c) the horizontal; note the oxide is tensile loaded to yielding (4.5 GPa) across most of the plane. From the loading curves (d), the yield stress at 0.2% strain was extracted (inset), as well as the work hardening exponent, n , from the true stress-strain curves (not plotted), indicating a proportionally much larger impact of the oxide layers on work hardening than on yielding.

Al₂O₃ varying Al–Al₂O₃ layering as in Fig. 1b, as well as the extrema of this sample: an Al–Al₂O₃ multilayer where all oxide layers are 1.2 nm thick, and another where these are all 12 nm thick. Illustrative deformation and stress fields at maximum applied strain are given in Fig. 10: the oxide layers are seen to exert a retaining lateral stress on the metallic layers, which increases with ceramic layer thickness, and could result in the yielding of these oxide layers within the total strain levels applied experimentally. The overall morphology of the deformed pillar in Fig. 10b,c is consistent with that experimentally observed in Fig. 5b at 15% strain, particularly when considering relative thickness of the Al layers as a function of position along the multilayer height and laterally relative to the centreline. Indeed, in both experiment and simulation, the lowest layer is thickest in the pillar centre, experiencing only a low axial strain, unlike at the pillar edges for this layer. This lateral strain heterogeneity per metal layer is inverted by the 4th and 5th layers, being more highly axially strained in the pillar centre than at the bulged edges, before becoming more laterally homogeneous upon progressing towards the diamond punch. Stress-strain curves were extracted from the reactive force of the Si base, and the relative displacement at each analysis step of the top and bottom surfaces of the Al–Al₂O₃ multilayer. The yield stress was extracted with a 0.2% offset criterion, and the work hardening parameter, n , was extracted from the true stress-strain, $\sigma_{\text{true}} - \epsilon_{\text{true}}$, data according to $\sigma_{\text{true}} = K \epsilon_{\text{true}}^n$ (K is the strength coefficient).

For the all-12 nm Al₂O₃ condition, the yield stress increase is highest, at 7 – 9% relative to the pure Al reference, depending on the exact yielding properties of the simulated Al material (see Experimental Methods); this yield increase reduces to only 4 – 5% for the specific multilayer arrangement experimentally studied here. However, these ~10–20 MPa strength gains as a result of the presence of the elastoplastic oxide layers are insufficient to explain

the observed strength improvements of over 100 MPa. Instead, the oxide layers, if they were to remain intact (which we know to not be the case above 5 nm thickness) would lead instead to an increased work hardening coefficient for higher oxide film thickness, Fig. 10. No substantial change in the elastic modulus was observed, based on the loading line: relative to the pure Al reference, the variation was of up to –3.0 to 3.5% across the range of multilayer and Al material property conditions tested. This result of FEM is reflected in particular by the success of the experimental Al–Al₂O₃ (0 – 1 nm) multilayer here in generating a strength increase of 73 MPa over the pure Al, notably for oxide layer thicknesses above 0.5 nm, despite the load bearing capability of such thin layers being low. Therefore, our attention should focus on the Al–Al₂O₃ interface as the source of strength – whether an impenetrable barrier or another mechanism, as discussed in the final section.

4.2.3. An additional strengthening mechanism

Given the above on plasticity transmission into thin hard ceramic layers, and the fact that the strengthening here is observed even at oxide layer thicknesses of 0.5 nm, suggests that impenetrable barrier theory is an incomplete description of the mechanisms active. It was observed, Fig. 5, that after compression the dislocation density was lower than before deformation, particularly in the grain centres. However, high resolution imaging of the regions near the oxide layers indicated several dislocation arms that appeared pinned on one end at the metal–oxide interface, Fig. 5h. It is currently unclear to what extent the crystalline–amorphous interface in this metal–ceramic hybrid may impact dislocation nucleation, mobility and annihilation: is it possible that the interface acts as a dislocation sink, whilst simultaneously resisting the nucleation of new Al dislocations from these grain boundary interfaces? In this case, heterogeneous dislocation nucleation would

only be favourable from the vertical grain boundaries, running perpendicular to the oxide layers. Experimental analysis of such plasticity, to capture slip continuity across Al GBs and oxide layers is envisageable by digital image correlation strain mapping, which has recently been applied to such microscale testpieces [94,95], now regularly achieving sub-100 nm resolutions, as low as 40 nm [96], even at high temperature [95,97,98]. Note that this sink characteristic would not necessarily be contradictory to the triple-point effects (intersection of vertical Al GBs with horizontal Al-Al₂O₃ interphase, Section 3.2.2) thought to lead to cracking of the >5 nm oxide as the magnitude of stress concentration here may still lie below those known to occur at all-crystalline metallic Al triple points [99].

In the crystalline/amorphous Cu/CuZr systems studied extensively over the past decade [100–103] both experimentally and by molecular dynamics simulation, shear transformation zones in the metallic glass are reported to co-locate with slip banding of the crystalline layers of usually equal thickness, whilst coarse shear banding of the CuZr can be suppressed. Such co-localised plasticity of the amorphous phase may well be activated in a-Al₂O₃ here due to the dense, flaw-less and easy bond-switching characteristics of the ALD-grown phase [41].

Searching in a different direction, the strength may result from a repression of grain boundary processes standardly active in UFG Al, such as grain boundary sliding and grain boundary diffusion. It is straightforward to imagine that the vertical boundaries in our system are not conducive to sliding processes as it is apparent here that the oxide layers are not shearable, nor is grain rotation easily accommodated. In the fine grained microstructures of PVD metals, the relatively clean grain boundaries, combined with a high vacancy density from deposition, means diffusion often dominates mechanics – be this for assisting dislocation nucleation by nuclei formation at a GB [104], GB sliding or creep. It may be hypothesised that here this major contribution of GB diffusion is limited to the vertical grain boundaries only, which as said cannot geometrically alone fulfil deformation: the metal-oxide interfaces produced by in situ shuttling between PVD and ALD deposition systems are expected to experience slower diffusion due to the increased covalent character of bonding. A strength limitation by slow diffusion at the Al-Al₂O₃ boundary would in theory [105] also lead to a small activation volume ($<10b^3$), as evoked here in the Supplementary Material. This interpretation is supported by recent nano-tensile loading of Al where 26 vol.% of the gauge was the surface natural oxide layer: dislocation motion in Al was heavily restricted by the interface with the oxide layer [106,107]. Electron beam irradiation reportedly led to rejuvenation of the amorphous oxide, leading to defecting of the oxide-metal interface and a transfer from internal dislocation multiplication to interface-dominated nucleation.

Further investigation of the (both metal/ceramic and crystalline/amorphous) Al/Al₂O₃ hybrid system by crystal plasticity FEM or discrete dislocation simulations could shed light on the role of the oxide layers. However, molecular dynamics modelling, currently underway, along with the correspondingly smaller size-scale experimental investigation of Al/Al₂O₃ multilayers (metallic layers ~5 – 25 nm thick), it is thought will better explain the mechanism of strengthening contributed by the continuous amorphous oxide layers, and establish the minimum oxide thickness to confer this. Such true nanolaminates would be expected to display a greater strengthening effect of the oxide layers than the ~100 MPa here, due to the greater role of interfaces in controlling plasticity at such smaller scales [12].

5. Conclusions

Microcompression of 250 nm/1 – 10 nm (nominal) Al/Al₂O₃ crystalline/amorphous multilayers identified homogenous co-

deformation of the layers, as well as barrelling of the individual metal layers at the micropillar edges. Where the true oxide layer thickness exceeded 5 nm, in-plane fracture of these layers was observed in few locations coincident with contact of vertical Al-Al grain boundaries with the Al-Al₂O₃ interphase; below this thickness, no fracture was seen. No failure or sliding at the Al-Al₂O₃ interface itself was found, unlike previously studied Al/ceramic systems where nearest-neighbour loss at the interface, and hence extrusion of the Al layers past the ceramic, was common. Upon further refining the oxide in the Al-Al₂O₃ (0 – 1 nm) multilayer, the role of the oxide layer in stabilising the pillar against lateral plasticity was found to be effective down to an oxide thickness of just ~0.5 nm. Deformation of the pure Al reference was consistent with literature for ultra-fine grained pure Al in both morphology and strength (425 MPa), where a high density of high angle boundaries was present. The Al/Al₂O₃ (1 – 10 nm) multilayers displayed a 107 MPa higher yield stress, which exceeded any oxide dispersion strengthening envisageable with the present volume fraction of oxide phase and scale of dispersion. This 532 MPa pseudo-macroscopic yield is competitive with most modern Al alloys – before any matrix strengthening or further grain refinement is considered. Alternative sources for this strength were considered: the in-plane tensile loading of the oxide layers resulting from their traction by the plasticity of the well-bonded Al layers was found to not contribute more than ~15 MPa to the yield strength, despite the high tensile strength and ductility of the thinner ALD Al₂O₃ layers – these more substantially impacted work hardening behaviour instead. Further investigation is required to elucidate the role of the crystalline-amorphous, metal-ceramic Al-Al₂O₃ hybrid interface in the mechanism of Al strengthening – it is possible that it is simply an impenetrable barrier, or that it acts as a dislocation sink, whilst the slow diffusion along the interface limits its dislocation nucleating ability.

Declaration of competing interest

The authors declare that they have no known competing financial interests or personal relationships that could have appeared to influence the work reported in this paper.

Acknowledgements

T.E.J.E. received funding from EMPAPOSTDOCS-II of the European Union's Horizon 2020 research and innovation programme under the Marie Skłodowska-Curie grant agreement number



754364. X.T. would like to acknowledge the funding from China Scholarship Council (CSC).

Supplementary materials

Supplementary material associated with this article can be found, in the online version, at doi:[10.1016/j.actamat.2022.118345](https://doi.org/10.1016/j.actamat.2022.118345).

Reference

- [1] Z. Wu, X. Chen, Y. Zhang, C. Dun, D.L. Carroll, Z. Hu, In Situ electrical Properties' investigation and nanofabrication of Ag/Sb₂Te₃ assembled Multilayers' film, *Adv. Mater. Interfaces* 5 (4) (2018) 1701210.
- [2] A. Cacucci, I. Tsiaoussis, V. Potin, L. Imhoff, N. Martin, T. Nyberg, The interdependence of structural and electrical properties in TiO₂/TiO/Ti periodic multilayers, *Acta Mater.* 61 (11) (2013) 4215–4225.
- [3] M. Albrecht, G. Hu, I.L. Guhr, T.C. Ulbrich, J. Boneberg, P. Leiderer, G. Schatz, Magnetic multilayers on nanospheres, *Nat. Mater.* 4 (3) (2005) 203–206.
- [4] T. Wang, H.-P. Ma, J.-G. Yang, J.-T. Zhu, H. Zhang, J. Feng, S.-J. Ding, H.-L. Lu, D.W. Zhang, Investigation of the optical and electrical properties of ZnO/Cu/ZnO multilayers grown by atomic layer deposition, *J. Alloys Compd.* 744 (2018) 381–385.

- [5] N. Li, M. Nastasi, A. Misra, Defect structures and hardening mechanisms in high dose helium ion implanted Cu and Cu/Nb multilayer thin films, *Int. J. Plast.* 32–33 (2012) 1–16.
- [6] M.J. Demkowicz, R.G. Hoagland, J.P. Hirth, Interface structure and radiation damage resistance in Cu-Nb multilayer nanocomposites, *Phys. Rev. Lett.* 100 (13) (2008) 136102.
- [7] E.G. Fu, J. Carter, G. Swadener, A. Misra, L. Shao, H. Wang, X. Zhang, Size dependent enhancement of helium ion irradiation tolerance in sputtered Cu/V nanolaminates, *J. Nucl. Mater.* 385 (3) (2009) 629–632.
- [8] S. Zheng, I.J. Beyerlein, J.S. Carpenter, K. Kang, J. Wang, W. Han, N.A. Mara, High-strength and thermally stable bulk nanolayered composites due to twin-induced interfaces, *Nat. Commun.* 4 (1) (2013) 1696.
- [9] X. Zhang, R.K. Schulze, H. Wang, A. Misra, Thermal stability of sputtered Cu/304 stainless steel multilayer films, *J. Appl. Phys.* 101 (12) (2007) 124311.
- [10] B. Putz, S. Wurster, T.E.J. Edwards, B. Völker, G. Milassin, D.M. Többs, C.O.A. Semprinoschnig, M.J. Cordill, Mechanical and optical degradation of flexible optical solar reflectors during simulated low earth orbit thermal cycling, *Acta Astronaut.* 175 (2020) 277–289.
- [11] C.R. Mayer, L.W. Yang, S.S. Singh, J. Llorca, J.M. Molina-Aldareguia, Y.L. Shen, N. Chawla, Anisotropy, size, and aspect ratio effects on micropillar compression of AlSiC nanolaminate composites, *Acta Mater.* 114 (2016) 25–32.
- [12] J. Wang, A. Misra, An overview of interface-dominated deformation mechanisms in metallic multilayers, *Curr. Opin. Solid State Mater. Sci.* 15 (1) (2011) 20–28.
- [13] R. Goswami, C.S. Pande, N. Bernstein, M.D. Johannes, C. Baker, G. Villalobos, A high degree of enhancement of strength of sputter deposited Al/Al₂O₃ multilayers upon post annealing, *Acta Mater.* 95 (2015) 378–385.
- [14] R. Raghavan, J.M. Wheeler, D. Esqué-de los Ojos, K. Thomas, E. Almandoz, G.G. Fuentes, J. Michler, Mechanical behavior of Cu/TiN multilayers at ambient and elevated temperatures: stress-assisted diffusion of Cu, *Mater. Sci. Eng. A Struct. Mater.* 620 (2015) 375–382.
- [15] L.W. Yang, C. Mayer, N. Li, J.K. Baldwin, N.A. Mara, N. Chawla, J.M. Molina-Aldareguia, J. Llorca, Mechanical properties of metal-ceramic nanolaminates: effect of constraint and temperature, *Acta Mater.* 142 (2018) 37–48.
- [16] Z.H. Cao, Y.P. Cai, C. Sun, Y.J. Ma, M.Z. Wei, Q. Li, H.M. Lu, H. Wang, X. Zhang, X.K. Meng, Tailoring strength and plasticity of Ag/Nb nanolaminates via intrinsic microstructure and extrinsic dimension, *Int. J. Plast.* 113 (2019) 145–157.
- [17] N.A. Mara, D. Bhattacharyya, P. Dickerson, R.G. Hoagland, A. Misra, Deformability of ultrahigh strength 5nm Cu/Nb nanolayered composites, *Appl. Phys. Lett.* 92 (23) (2008) 231901.
- [18] T. Xie, J. Zhu, L. Fu, R. Zhang, N. Li, M. Yang, J. Wang, W. Qin, W. Yang, D. Li, L. Zhou, The evolution of hardness in Cu-W alloy thin films, *Mater. Sci. Eng. A Struct. Mater.* 729 (2018) 170–177.
- [19] Y.Y. Lu, R. Kotoka, J.P. Ligda, B.B. Cao, S.N. Yarmolenko, B.E. Schuster, Q. Wei, The microstructure and mechanical behavior of Mg/Ti multilayers as a function of individual layer thickness, *Acta Mater.* 63 (2014) 216–231.
- [20] J.W. Yan, G.P. Zhang, X.F. Zhu, H.S. Liu, C. Yan, Microstructures and strengthening mechanisms of Cu/Ni/W nanolayered composites, *Philos. Mag.* 93 (5) (2013) 434–448.
- [21] D. Bhattacharyya, N.A. Mara, P. Dickerson, R.G. Hoagland, A. Misra, Compressive flow behavior of Al-TiN multilayers at nanometer scale layer thickness, *Acta Mater.* 59 (10) (2011) 3804–3816.
- [22] I. Salehinia, J. Wang, D.F. Bahr, H.M. Zbib, Molecular dynamics simulations of plastic deformation in Nb/NbC multilayers, *Int. J. Plast.* 59 (2014) 119–132.
- [23] J. Wang, C. Zhou, I.J. Beyerlein, S. Shao, Modeling interface-dominated mechanical behavior of Nanolayered crystalline composites, *JOM* 66 (1) (2014) 102–113.
- [24] S. Shao, H.M. Zbib, I.N. Mastorakos, D.F. Bahr, Deformation mechanisms, size effects, and strain hardening in nanoscale metallic multilayers under nanoindentation, *J. Appl. Phys.* 112 (4) (2012) 044307.
- [25] J.Y. Zhang, X. Zhang, G. Liu, G.J. Zhang, J. Sun, Scaling of the ductility with yield strength in nanostructured Cu/Cr multilayer films, *Scr. Mater.* 63 (1) (2010) 101–104.
- [26] Y. Liu, D. Bufford, S. Rios, H. Wang, J. Chen, J.Y. Zhang, X. Zhang, A formation mechanism for ultra-thin nanotwins in highly textured Cu/Ni multilayers, *J. Appl. Phys.* 111 (7) (2012) 073526.
- [27] A. Misra, J.P. Hirth, R.G. Hoagland, Length-scale-dependent deformation mechanisms in incoherent metallic multilayered composites, *Acta Mater.* 53 (18) (2005) 4817–4824.
- [28] Y.F. Zhang, S. Xue, Q. Li, J. Li, J. Ding, T.J. Niu, R. Su, H. Wang, X. Zhang, Size dependent strengthening in high strength nanotwinned Al/Ti multilayers, *Acta Mater.* 175 (2019) 466–476.
- [29] A. Kelling, K.R. Mangipudi, I. Knorr, T. Liese, H.-U. Krebs, C.A. Volkert, Investigating fracture of nanoscale metal-ceramic multilayers in the transmission electron microscope, *Scr. Mater.* 115 (2016) 42–45.
- [30] I. Salehinia, S. Shao, J. Wang, H.M. Zbib, Plastic deformation of Metal/Ceramic Nanolayered composites, *JOM* 66 (10) (2014) 2078–2085.
- [31] M. Wang, D. Wang, T. Kups, P. Schaaf, Size effect on mechanical behavior of Al/Si₃N₄ multilayers by nanoindentation, *Mater. Sci. Eng. A Struct. Mater.* 644 (2015) 275–283.
- [32] S. Lotfian, M. Rodríguez, K.E. Yazzie, N. Chawla, J. Llorca, J.M. Molina-Aldareguia, High temperature micropillar compression of Al/SiC nanolaminates, *Acta Mater.* 61 (12) (2013) 4439–4451.
- [33] D.R.P. Singh, N. Chawla, G. Tang, Y.L. Shen, Micropillar compression of Al/SiC nanolaminates, *Acta Mater.* 58 (20) (2010) 6628–6636.
- [34] R. Kumar, L. Nicola, E. Van der Giessen, Density of grain boundaries and plasticity size effects: A discrete dislocation dynamics study, *Mater. Sci. Eng. A Struct. Mater.* 527 (1) (2009) 7–15.
- [35] L. Nicola, E. Van der Giessen, A. Needleman, Size effects in polycrystalline thin films analyzed by discrete dislocation plasticity, *Thin. Solid. Films* 479 (1) (2005) 329–338.
- [36] K.M. Davoudi, J.J. Vlassak, Dislocation evolution during plastic deformation: equations vs. discrete dislocation dynamics study, *J. Appl. Phys.* 123 (8) (2018) 085302.
- [37] S. Lotfian, C. Mayer, N. Chawla, J. Llorca, A. Misra, J.K. Baldwin, J.M. Molina-Aldareguia, Effect of layer thickness on the high temperature mechanical properties of Al/SiC nanolaminates, *Thin. Solid. Films* 571 (2014) 260–267.
- [38] R. Raghavan, J.M. Wheeler, T.P. Harzer, V. Chawla, S. Djaziri, K. Thomas, B. Philippi, C. Kirchlechner, B.N. Jaya, J. Wehrs, J. Michler, G. Dehm, Transition from shear to stress-assisted diffusion of copper-chromium nanolayered thin films at elevated temperatures, *Acta Mater.* 100 (2015) 73–80.
- [39] L.W. Yang, C. Mayer, N. Chawla, J. Llorca, J.M. Molina-Aldareguia, Deformation mechanisms of ultra-thin Al layers in Al/SiC nanolaminates as a function of thickness and temperature, *Philos. Mag.* 96 (32–34) (2016) 3336–3355.
- [40] N. Li, H. Wang, A. Misra, J. Wang, In situ nanoindentation study of plastic co-deformation in Al-TiN nanocomposites, *Sci. Rep.* 4 (1) (2014) 6633.
- [41] E.J. Frankberg, J. Kalikka, F. García Ferré, L. Joly-Pottuz, T. Salminen, J. Hintikka, M. Hokka, S. Koneiti, T. Douillard, B. Le Saint, P. Kreiml, M.J. Cordill, T. Epicier, D. Stauffer, M. Vanazzi, L. Roiban, J. Akola, F. Di Fonzo, E. Levänen, K. Masenelli-Varlot, Highly ductile amorphous oxide at room temperature and high strain rate, *Science* 366 (6467) (2019) 864–869.
- [42] W.X.K.J.W. Lee, C. J. Hone, Measurement of the elastic properties and intrinsic strength of monolayer graphene, *Science* 321 (5887) (2008) 385.
- [43] Y. Kim, J. Lee, M.S. Yeom, J.W. Shin, H. Kim, Y. Cui, J.W. Kysar, J. Hone, Y. Jung, S. Jeon, S.M. Han, Strengthening effect of single-atomic-layer graphene in metal-graphene nanolayered composites, *Nat. Commun.* 4 (1) (2013) 2114.
- [44] T. Xie, T.E.J. Edwards, N.M. della Ventura, D. Casari, E. Huzsár, L. Fu, L. Zhou, X. Maeder, J.J. Schwiedrzik, I. Utke, J. Michler, L. Pethö, Synthesis of model Al-Al₂O₃ multilayer systems with monolayer oxide thickness control by circumventing native oxidation, *Thin. Solid. Films* 711 (2020) 138287.
- [45] J. Acharya, J. Wilt, B. Liu, J. Wu, Probing the dielectric properties of ultrathin Al/Al₂O₃/Al trilayers fabricated using in situ sputtering and atomic layer deposition, *ACS Appl. Mater. Interfaces* 10 (3) (2018) 3112–3120.
- [46] D. Kiener, C. Motz, G. Dehm, Micro-compression testing: A critical discussion of experimental constraints, *Mater. Sci. Eng. A Struct. Mater.* 505 (1) (2009) 79–87.
- [47] H. Zhang, B.E. Schuster, Q. Wei, K.T. Ramesh, The design of accurate micro-compression experiments, *Scr. Mater.* 54 (2) (2006) 181–186.
- [48] V. Rontu, A. Nölvä, A. Hokkanen, E. Haegström, I. Kassamakov, S. Franssila, Elastic and fracture properties of free-standing amorphous ALD Al₂O₃ thin films measured with bulge test, *Mater. Res. Express* 5 (4) (2018) 046411.
- [49] J. Proost, F. Spaepen, Evolution of the growth stress, stiffness, and microstructure of alumina thin films during vapor deposition, *J. Appl. Phys.* 91 (1) (2002) 204–216.
- [50] M.A. Hopcroft, W.D. Nix, T.W. Kenny, What is the Young's modulus of silicon? *J. Microelectromech. Syst.* 19 (2) (2010) 229–238.
- [51] S.M. Han, M.A. Phillips, W.D. Nix, Study of strain softening behavior of Al-Al₃Sc multilayers using microcompression testing, *Acta Mater.* 57 (15) (2009) 4473–4490.
- [52] Y.S. Choi, K.I. Kim, K.H. Oh, H.N. Han, S.H. Kang, J. Jang, J.H. Han, Dynamic recrystallization in high-purity aluminum single crystal under frictionless deformation mode at room temperature, *J. Mater. Res.* 28 (20) (2013) 2829–2834.
- [53] J.T. Pürstl, H.O. Jones, T.E.J. Edwards, R.P. Thompson, F. Di Gioacchino, N.G. Jones, W.J. Clegg, On the extraction of yield stresses from micro-compression experiments, *Mater. Sci. Eng. A Struct. Mater.* 800 (2021) 140323.
- [54] A.S. Krausz, A deformation kinetics analysis of the stress sensitivity, *Mater. Sci. Eng. R Rep.* 26 (1) (1976) 65–71.
- [55] G. Schoeck, The activation energy of dislocation movement, *Phys. Status Solidi B Basic Solid State Phys.* 8 (2) (1965) 499–507.
- [56] Y. Xiao, V. Maier-Kiener, J. Michler, R. Spolenak, J.M. Wheeler, Deformation behavior of aluminum pillars produced by Xe and Ga focused ion beams: Insights from strain rate jump tests, *Mater. Design* 181 (2019) 107914.
- [57] Q. Li, S. Xue, Y. Zhang, X. Sun, H. Wang, X. Zhang, Plastic anisotropy and tension-compression asymmetry in nanotwinned Al-Fe alloys: An in-situ micro-mechanical investigation, *Int. J. Plast.* 132 (2020) 102760.
- [58] Y. Xiao, J. Wehrs, H. Ma, T. Al-Samman, S. Korte-Kerzel, M. Göken, J. Michler, R. Spolenak, J.M. Wheeler, Investigation of the deformation behavior of aluminum micropillars produced by focused ion beam machining using Ga and Xe ions, *Scr. Mater.* 127 (2017) 191–194.
- [59] Q. Li, S. Xue, J. Wang, S. Shao, A.H. Kwong, A. Giwa, Z. Fan, Y. Liu, Z. Qi, J. Ding, H. Wang, J.R. Greer, H. Wang, X. Zhang, High-strength nanotwinned Al alloys with 9R phase, *Adv. Mater.* 30 (11) (2018) 1704629.
- [60] H.-T. Li, L.-F. Chen, X. Yuan, W.-Q. Zhang, J.R. Smith, A.G. Evans, Interfacial stoichiometry and adhesion at metal/ α -Al₂O₃ interfaces, *J. Am. Ceram. Soc.* 94 (s1) (2011) s154–s159.
- [61] C. Guerra-Núñez, M. Döbeli, J. Michler, I. Utke, Reaction and growth mechanisms in Al₂O₃ deposited via atomic layer deposition: elucidating the hydrogen source, *Chem. Mater.* 29 (20) (2017) 8690–8703.
- [62] D.J. Siegel, L.G. Hector, J.B. Adams, Ab initio study of Al-ceramic interfacial adhesion, *Phys. Rev. B* 67 (9) (2003) 092105.

- [63] C.R. Dandekar, Y.C. Shin, Molecular dynamics based cohesive zone law for describing Al–SiC interface mechanics, *Compos., Part A* 42 (4) (2011) 355–363.
- [64] B. Ohler, S. Prada, G. Pacchioni, W. Langel, DFT simulations of titanium oxide films on titanium metal, *J. Phys. Chem. C* 117 (1) (2013) 358–367.
- [65] D. Bhattacharyya, N.A. Mara, P. Dickerson, R.G. Hoagland, A. Misra, A transmission electron microscopy study of the deformation behavior underneath nanoindents in nanoscale Al–TiN multilayered composites, *Philos. Mag.* 90 (13) (2010) 1711–1724.
- [66] N.A. Mara, D. Bhattacharyya, J.P. Hirth, P. Dickerson, A. Misra, Mechanism for shear banding in nanolayered composites, *Appl. Phys. Lett.* 97 (2) (2010) 021909.
- [67] J.Y. Zhang, G. Liu, S.Y. Lei, J.J. Niu, J. Sun, Transition from homogeneous-like to shear-band deformation in nanolayered crystalline Cu/amorphous Cu–Zr micropillars: intrinsic vs. extrinsic size effect, *Acta Mater.* 60 (20) (2012) 7183–7196.
- [68] J. May, H.W. Höppel, M. Göken, Strain rate sensitivity of ultrafine-grained aluminium processed by severe plastic deformation, *Scr. Mater.* 53 (2) (2005) 189–194.
- [69] J.M. Staehler, W.W. Predebon, B.J. Pletka, G. Subhash, Strain-rate effects in high-purity alumina, *JOM* 47 (5) (1995) 60–63.
- [70] R.W. Kozar, A. Suzuki, W.W. Milligan, J.J. Schirra, M.F. Savage, T.M. Pollock, Strengthening mechanisms in polycrystalline multimodal nickel-base superalloys, *Metall. Mat. Trans. A* 40 (7) (2009) 1588–1603.
- [71] A.J. Ardell, Precipitation hardening, *MTA* 16 (12) (1985) 2131–2165.
- [72] T.J. Koppenaal, D. Kuhlmann-Wilsdorf, The effect of prestressing on the strength of neutron-irradiated copper single crystals, *Appl. Phys. Lett.* 4 (3) (1964) 59–61.
- [73] K. Kamoshida, Argon entrapment in magnetron-sputtered Al alloy films, *Thin. Solid. Films* 283 (1) (1996) 57–60.
- [74] E.O. Hall, The deformation and ageing of mild steel: III Discussion of results, *Proc. Phys. Soc. Lond. Sect. B* 64 (9) (1951) 747–753.
- [75] N. Petch, The cleavage strength of polycrystals, *J. Iron Steel Inst.* 174 (1953) 25–28.
- [76] N. Kamikawa, X. Huang, N. Tsuji, N. Hansen, Strengthening mechanisms in nanostructured high-purity aluminium deformed to high strain and annealed, *Acta Mater.* 57 (14) (2009) 4198–4208.
- [77] K. Maung, J.C. Earthman, F.A. Mohamed, Inverse Hall–Petch behavior in diamondane stabilized bulk nanocrystalline aluminum, *Acta Mater.* 60 (16) (2012) 5850–5857.
- [78] N. Hansen, The effect of grain size and strain on the tensile flow stress of aluminium at room temperature, *Acta Metall.* 25 (8) (1977) 863–869.
- [79] Z.C. Cordero, B.E. Knight, C.A. Schuh, Six decades of the Hall–Petch effect – a survey of grain-size strengthening studies on pure metals, *Int. Mater. Rev.* 61 (8) (2016) 495–512.
- [80] L.P. Evers, D.M. Parks, W.A.M. Brekelmans, M.G.D. Geers, Crystal plasticity model with enhanced hardening by geometrically necessary dislocation accumulation, *J. Mech. Phys. Solids* 50 (11) (2002) 2403–2424.
- [81] J. Jiang, T.B. Britton, A.J. Wilkinson, Evolution of dislocation density distributions in copper during tensile deformation, *Acta Mater.* 61 (19) (2013) 7227–7239.
- [82] M.J. Hordon, B.L. Averbach, X-ray measurements of dislocation density in deformed Copper and Aluminum single crystals, *Acta Metall.* 9 (3) (1961) 237–246.
- [83] G. Csiszár, L. Balogh, A. Misra, X. Zhang, T. Ungár, The dislocation density and twin-boundary frequency determined by X-ray peak profile analysis in cold rolled magnetron-sputter deposited nanotwinned copper, *J. Appl. Phys.* 110 (4) (2011) 043502.
- [84] Q. Li, J. Cho, S. Xue, X. Sun, Y. Zhang, Z. Shang, H. Wang, X. Zhang, High temperature thermal and mechanical stability of high-strength nanotwinned Al alloys, *Acta Mater.* 165 (2019) 142–152.
- [85] C.Q. Chen, Y.T. Pei, J.T.M. De Hosson, Effects of size on the mechanical response of metallic glasses investigated through in situ TEM bending and compression experiments, *Acta Mater.* 58 (1) (2010) 189–200.
- [86] O. Glushko, M. Mühlbacher, C. Gammer, M.J. Cordill, C. Mitterer, J. Eckert, Exceptional fracture resistance of ultrathin metallic glass films due to an intrinsic size effect, *Sci. Rep.* 9 (1) (2019) 8281.
- [87] A.T. Alpas, J.D. Embury, D.A. Hardwick, R.W. Springer, The mechanical properties of laminated microscale composites of Al/Al₂O₃, *J. Mater. Sci.* 25 (3) (1990) 1603–1609.
- [88] M.P. de Boer, A.D. Corwin, P.G. Kotula, M.S. Baker, J.R. Michael, G. Subhash, M.J. Shaw, On-chip laboratory suite for testing of free-standing metal film mechanical properties, Part II – experiments, *Acta Mater.* 56 (14) (2008) 3313–3326.
- [89] D. Bhattacharyya, N.A. Mara, R.G. Hoagland, A. Misra, Nanoindentation and microstructural studies of Al/TiN multilayers with unequal volume fractions, *Scr. Mater.* 58 (11) (2008) 981–984.
- [90] J.M. Wheeler, C. Harvey, N. Li, A. Misra, N.A. Mara, X. Maeder, J. Michler, S. Pathak, High temperature nanoindentation of Cu–TiN nanolaminates, *Mater. Sci. Eng. A Struct. Mater.* 804 (2021) 140522.
- [91] H.-C. Tsai, Compression analysis of rectangular elastic layers bonded between rigid plates, *Int. J. Solids Struct.* 42 (11) (2005) 3395–3410.
- [92] S. Qiao, N. Lu, Analytical solutions for bonded elastically compressible layers, *Int. J. Solids Struct.* 58 (2015) 353–365.
- [93] W.G. Beare, F.P. Bowden, T.M. Lowry, Physical properties of surfaces I - Kinetic friction, *Philos. Trans. A Math. Phys. Eng. Sci.* 234 (741) (1935) 329–354.
- [94] F. Di Gioacchino, W.J. Clegg, Mapping deformation in small-scale testing, *Acta Mater.* 78 (2014) 103–113.
- [95] T.E.J. Edwards, F. Di Gioacchino, G. Mohanty, J. Wehrs, J. Michler, W.J. Clegg, Longitudinal twinning in a TiAl alloy at high temperature by in situ micro-compression, *Acta Mater.* 148 (2018) 202–215.
- [96] A. Orozco-Caballero, D. Lunt, J.D. Robson, J. Quinta da Fonseca, How magnesium accommodates local deformation incompatibility: A high-resolution digital image correlation study, *Acta Mater.* 133 (2017) 367–379.
- [97] T.E.J. Edwards, F. Di Gioacchino, H.P. Springbett, R.A. Oliver, W.J. Clegg, Stable speckle patterns for nano-scale strain mapping up to 700°C, *Exp. Mech.* 57 (2017) 1289–1309.
- [98] T.E.J. Edwards, F. Di Gioacchino, W.J. Clegg, An experimental study of polycrystalline plasticity in lamellar titanium aluminide, *Int. J. Plast.* 118 (2019).
- [99] K.T. Hong, S.W. Nam, Cyclic stress effects on the grain boundary cracking in Al–Mg solid solution, *J. Mater. Sci.* 23 (4) (1988) 1171–1181.
- [100] W. Guo, E. Jägle, J. Yao, V. Maier, S. Korte-Kerzel, J.M. Schneider, D. Raabe, Intrinsic and extrinsic size effects in the deformation of amorphous CuZr/nanocrystalline Cu nanolaminates, *Acta Mater.* 80 (2014) 94–106.
- [101] B. Brandl, T.C. Germann, A. Misra, Structure and shear deformation of metallic crystalline–amorphous interfaces, *Acta Mater.* 61 (10) (2013) 3600–3611.
- [102] B. Cheng, J.R. Trelewicz, Mechanistic coupling of dislocation and shear transformation zone plasticity in crystalline–amorphous nanolaminates, *Acta Mater.* 117 (2016) 293–305.
- [103] B. Cheng, J.R. Trelewicz, Design of crystalline–amorphous nanolaminates using deformation mechanism maps, *Acta Mater.* 153 (2018) 314–326.
- [104] R.J. Asaro, S. Suresh, Mechanistic models for the activation volume and rate sensitivity in metals with nanocrystalline grains and nano-scale twins, *Acta Mater.* 53 (12) (2005) 3369–3382.
- [105] A.G. Evans, R.D. Rawlings, The thermally activated deformation of crystalline materials, *Phys. Status Solidi B Basic Solid State Phys.* 34 (1) (1969) 9–31.
- [106] S.-H. Li, W.-Z. Han, J. Li, E. Ma, Z.-W. Shan, Small-volume aluminum alloys with native oxide shell deliver unprecedented strength and toughness, *Acta Mater.* 126 (2017) 202–209.
- [107] S.-H. Li, W.-Z. Han, Z.-W. Shan, Deformation of small-volume Al–4Cu alloy under electron beam irradiation, *Acta Mater.* 141 (2017) 183–192.
- [108] R.W. Hayes, D. Witkin, F. Zhou, E.J. Lavernia, Deformation and activation volumes of cryomilled ultrafine-grained aluminum, *Acta Mater.* 52 (14) (2004) 4259–4271.
- [109] G.J. Raab, R.Z. Valiev, T.C. Lowe, Y.T. Zhu, Continuous processing of ultrafine grained Al by ECAP–Conform, *Mater. Sci. Eng. A Struct. Mater.* 382 (1) (2004) 30–34.
- [110] N. Tsuji, Y. Ito, Y. Saito, Y. Minamino, Strength and ductility of ultrafine grained aluminum and iron produced by ARB and annealing, *Scr. Mater.* 47 (12) (2002) 893–899.